

REPORT DOCUMENTATION PAGE			Form Approved OMB NO. 0704-0188		
<p>The public reporting burden for this collection of information is estimated to average 1 hour per response, including the time for reviewing instructions, searching existing data sources, gathering and maintaining the data needed, and completing and reviewing the collection of information. Send comments regarding this burden estimate or any other aspect of this collection of information, including suggestions for reducing this burden, to Washington Headquarters Services, Directorate for Information Operations and Reports, 1215 Jefferson Davis Highway, Suite 1204, Arlington VA, 22202-4302. Respondents should be aware that notwithstanding any other provision of law, no person shall be subject to any penalty for failing to comply with a collection of information if it does not display a currently valid OMB control number.</p> <p>PLEASE DO NOT RETURN YOUR FORM TO THE ABOVE ADDRESS.</p>					
1. REPORT DATE (DD-MM-YYYY) 11-04-2008		2. REPORT TYPE Final Report		3. DATES COVERED (From - To) 1-Oct-2006 - 31-Mar-2008	
4. TITLE AND SUBTITLE Spin-Precession Organic Magnetic Sensor			5a. CONTRACT NUMBER		
			5b. GRANT NUMBER W911NF-06-C-0183		
			5c. PROGRAM ELEMENT NUMBER 7D10T2		
6. AUTHORS Srini Krishnamurthy			5d. PROJECT NUMBER		
			5e. TASK NUMBER		
			5f. WORK UNIT NUMBER		
7. PERFORMING ORGANIZATION NAMES AND ADDRESSES SRI International 333 Ravenswood Ave., Menlo Park, CA 94025 -			8. PERFORMING ORGANIZATION REPORT NUMBER		
9. SPONSORING/MONITORING AGENCY NAME(S) AND ADDRESS(ES) U.S. Army Research Office P.O. Box 12211 Research Triangle Park, NC 27709-2211			10. SPONSOR/MONITOR'S ACRONYM(S) ARO		
			11. SPONSOR/MONITOR'S REPORT NUMBER(S) 51974-EL-DRP.1		
12. DISTRIBUTION AVAILABILITY STATEMENT Approved for Public Release; Distribution Unlimited					
13. SUPPLEMENTARY NOTES The views, opinions and/or findings contained in this report are those of the author(s) and should not be construed as an official Department of the Army position, policy or decision, unless so designated by other documentation.					
14. ABSTRACT The three major tasks we addressed in this project were to: (a) identify the issues for demonstration of a polymer-based spin-precession magnetic sensor; (b) develop theoretical and computational techniques to study the effect of the interface between ferromagnetic metal and polymers for FET applications; and (c) apply the existing light propagation codes to study transmission of 1.5 μm wavelength light through GaAs. We have completed all three tasks, and the major results of our 18-month effort are: (1) Detailed device modeling confirms that a room temperature detectivity of ~ 50 fT/√Hz is possible with an appropriately					
15. SUBJECT TERMS magnetic sensor, spin FET, half metal, spin precession					
16. SECURITY CLASSIFICATION OF:		17. LIMITATION OF ABSTRACT SAR	15. NUMBER OF PAGES	19a. NAME OF RESPONSIBLE PERSON Srini Krishnamurthy	
a. REPORT U	b. ABSTRACT U			c. THIS PAGE U	19b. TELEPHONE NUMBER 650-859-4997

Report Title

Spin-Precession Organic Magnetic Sensor

ABSTRACT

The three major tasks we addressed in this project were to: (a) identify the issues for demonstration of a polymer-based spin-precession magnetic sensor; (b) develop theoretical and computational techniques to study the effect of the interface between ferromagnetic metal and polymers for FET applications; and (c) apply the existing light propagation codes to study transmission of 1.5 μm wavelength light through GaAs. We have completed all three tasks, and the major results of our 18-month effort are:

- (1) Detailed device modeling confirms that a room temperature detectivity of $\sim 50 \text{ fT}/\text{Hz}$ is possible with an appropriately fabricated polymer magnetic sensor.
- (2) Self-consistent charge and spin transport calculations indicate that doping concentrations and field-dependent mobility in the polymer and Schottky barrier height with the contacts can be optimized for enhanced field effect transistor performance and magnetic sensor sensitivity.
- (3) $\text{La}_{0.7}\text{Sr}_{0.3}\text{MnO}_3$ (LSMO) is demonstrated to be a ferromagnetic metal at room temperature.
- (4) Focused ion beam (FIB) lithography has been used to fabricate ultra-narrow trenches required for high-performance magnetic sensors, but the use of Ga^+ ions in the FIB oxidizes the ferromagnetic surface and prevents spin or charge injection from half-metal $\text{La}_{0.7}\text{Sr}_{0.3}\text{MnO}_3$ (LSMO).
- (5) We demonstrated the synthesis of very low mobility but heavily doped polymers and used them in magnetic sensor fabrication.
- (6) We calculated two-photon and free carrier absorption coefficients and changes to the refractive index used in light propagation codes and concluded that GaInAs alloy is a better limiting material at 1.5 μm than GaAs.

This report discusses our results and conclusions on key requirements.

List of papers submitted or published that acknowledge ARO support during this reporting period. List the papers, including journal references, in the following categories:

(a) Papers published in peer-reviewed journals (N/A for none)

None

Number of Papers published in peer-reviewed journals: 0.00

(b) Papers published in non-peer-reviewed journals or in conference proceedings (N/A for none)

None

Number of Papers published in non peer-reviewed journals: 0.00

(c) Presentations

None

Number of Presentations: 0.00

Non Peer-Reviewed Conference Proceeding publications (other than abstracts):

None

Number of Non Peer-Reviewed Conference Proceeding publications (other than abstracts): 0

Peer-Reviewed Conference Proceeding publications (other than abstracts):

None

Number of Peer-Reviewed Conference Proceeding publications (other than abstracts): 0

(d) Manuscripts

Self-consistent spin-charge transport in organic device structures

Realistic modeling of nonlinear absorption and transmission in semiconductor alloys

Number of Manuscripts: 2.00

Number of Inventions:

Graduate Students

<u>NAME</u>	<u>PERCENT SUPPORTED</u>
FTE Equivalent:	
Total Number:	

Names of Post Doctorates

<u>NAME</u>	<u>PERCENT SUPPORTED</u>
FTE Equivalent:	
Total Number:	

Names of Faculty Supported

<u>NAME</u>	<u>PERCENT SUPPORTED</u>
FTE Equivalent:	
Total Number:	

Names of Under Graduate students supported

<u>NAME</u>	<u>PERCENT SUPPORTED</u>
FTE Equivalent:	
Total Number:	

Student Metrics

This section only applies to graduating undergraduates supported by this agreement in this reporting period

- The number of undergraduates funded by this agreement who graduated during this period: 0.00
 - The number of undergraduates funded by this agreement who graduated during this period with a degree in science, mathematics, engineering, or technology fields:..... 0.00
 - The number of undergraduates funded by your agreement who graduated during this period and will continue to pursue a graduate or Ph.D. degree in science, mathematics, engineering, or technology fields:..... 0.00
 - Number of graduating undergraduates who achieved a 3.5 GPA to 4.0 (4.0 max scale):..... 0.00
 - Number of graduating undergraduates funded by a DoD funded Center of Excellence grant for Education, Research and Engineering:..... 0.00
 - The number of undergraduates funded by your agreement who graduated during this period and intend to work for the Department of Defense 0.00
 - The number of undergraduates funded by your agreement who graduated during this period and will receive scholarships or fellowships for further studies in science, mathematics, engineering or technology fields: 0.00
-

Names of Personnel receiving masters degrees

NAME

Total Number:

Names of personnel receiving PHDs

NAME

Total Number:

Names of other research staff

NAME

PERCENT_SUPPORTED

FTE Equivalent:

Total Number:

Sub Contractors (DD882)

Inventions (DD882)

Final Report • March 2008

SPIN-PRECESSION ORGANIC MAGNETIC SENSOR

ARO Project W911NF-06-C-0183
SRI Project P17826/P18031

Prepared by:

Srini Krishnamurthy
Principal Scientist
Applied Optics Laboratory

Prepared for:

U.S. Army Research Office
P.O. Box 12211
Research Triangle Park, NC 27709-2211

Attention: Dr. John Zavada

Approved by:

Robert Brown, Director
Applied Optics Laboratory

CONTENTS

EXECUTIVE SUMMARY	1
TECHNICAL DISCUSSION.....	2
1. Spin-Precession Magnetic Sensor.....	2
1.1 Device Concept and Operation.....	2
1.2 Objectives	2
1.3 LSMO Growth and Characterization.....	3
1.4 Fabrication of Nanotrenches.....	3
1.5 Polymer Synthesis.....	4
1.6 Noise Modeling.....	7
1.7 Improved Spin and Charge Transport Modeling	13
1.8 Performance Modeling.....	14
1.9 Conclusions.....	17
2. Field Effect Transistor	18
2.1 Schottky Barrier	19
2.2 Electric-Field Dependent Mobility	20
2.3 Transport Equations	20
2.4 Results.....	20
3. Light Propagation in GaAs	24
APPENDIX A.....	A-1
APPENDIX B	B-1

EXECUTIVE SUMMARY

The three major tasks we addressed in this project were to: (a) identify the issues for demonstration of a polymer-based spin-precession magnetic sensor; (b) develop theoretical and computational techniques to study the effect of the interface between ferromagnetic metal and polymers for FET applications; and (c) apply the existing light propagation codes to study transmission of 1.5 μm wavelength light through GaAs. We have completed all three tasks, and the major results of our 18-month effort are:

- (1) Detailed device modeling confirms that a room temperature detectivity of $\sim 50 \text{ fT}/\sqrt{\text{Hz}}$ is possible with an appropriately fabricated polymer magnetic sensor.
- (2) Self-consistent charge and spin transport calculations indicate that doping concentrations and field-dependent mobility in the polymer and Schottky barrier height with the contacts can be optimized for enhanced field effect transistor performance and magnetic sensor sensitivity.
- (3) $\text{La}_{0.7}\text{Sr}_{0.3}\text{MnO}_3$ (LSMO) is demonstrated to be a ferromagnetic metal at room temperature.
- (4) Focused ion beam (FIB) lithography has been used to fabricate ultra-narrow trenches required for high-performance magnetic sensors, but the use of Ga^+ ions in the FIB oxidizes the ferromagnetic surface and prevents spin or charge injection from half-metal $\text{La}_{0.7}\text{Sr}_{0.3}\text{MnO}_3$ (LSMO).
- (5) We demonstrated the synthesis of very low mobility but heavily doped polymers and used them in magnetic sensor fabrication.
- (6) We calculated two-photon and free carrier absorption coefficients and changes to the refractive index used in light propagation codes and concluded that GaInAs alloy is a better limiting material at 1.5 μm than GaAs.

This report discusses our results and conclusions on key requirements.

TECHNICAL DISCUSSION

1. SPIN-PRECESSION MAGNETIC SENSOR

This report summarizes the work accomplished from October 2006 through March 2008. The main objective of this work was to identify the issues related to realizing a polymer-based magnetic sensor with ultra-high detectivity at room temperature. Identification of the issues required full-fledged modeling, fabrication, and testing. In an effort to leverage the findings, the Office of Naval Research (ONR) funded another iteration of fabrication and testing. To provide continuity and completeness, this report comprehensively summarizes the results achieved under both programs.

1.1 Device Concept and Operation

The proposed device is a planar structure that uses half-metal $\text{La}_{0.7}\text{Sr}_{0.3}\text{MnO}_3$ (LSMO) for the contacts and an organic material for electron transport. The contacts are magnetically poled to have parallel magnetization. The half-metal nature of the contact allows injection of only one kind of spin (which is parallel to the magnetization) into the organic material. The constituents of the organics are usually atoms with small atomic numbers (such as H, C, N, O, and S), and the spin-orbit coupling is extremely small, which allows the injected spins to stay coherent for long periods. In the absence of any magnetic field, the injected electrons will retain the spin and can find a state in the other contact. However, when a magnetic field is applied, the electron spin will precess and the spin orientation with the contact magnetization will change, resulting in an increased resistance. Since a very small magnetic field is required to alter the electron spin orientation, the device is predicted to have very high sensitivity, even when operated at room temperature.

1.2 Objectives

The objectives of this seedling effort are to

- (1) Carry out more detailed modeling, based on self-consistent spin transport through the polymers, and predict the highest achievable sensitivity of organic magnetic sensors at room temperature.
- (2) Identify the technical challenges related to device fabrication and performance, such as room temperature performance of half-metal and its contact resistance; organic material synthesis, deposition and wetting; e-beam etching for nanotrenches in half metals; and injection efficiency of carriers from half-metal to organic material.
- (3) Identify the sources of noise, evaluate their effect on low-frequency and room temperature noise performance of organic magnetic sensors, and identify the technical challenges for improving signal-to-noise performance.

1.3 LSMO Growth and Characterization

LSMO layers were grown at Arizona State University by Professor Nathan Newman and his workers. The growth procedure used the pulsed laser deposition (PLD) technique, with oxygen working pressure of 350 mTorr, substrate temperature 600°C, laser power 450 mJ, frequency 2 Hz, and substrate-target distance ~5 cm. The duration of the growth is 2.5 h to obtain 300-nm-thick LSMO. The grown film was cooled down in a chamber with oxygen at a pressure of ~10 Torr and a cooling speed of ~10 K/min. No further treatment was done on the as-grown LaSrMnO₃ films. To verify the effect on the Curie temperature (T_c), two more batches of samples were grown in nearly identical conditions, with only the substrate temperature changed by $\pm 50^\circ\text{C}$.

We characterized the composition of the LSMO samples using Rutherford backscattering spectroscopy (RBS) and found it to be very close to the target composition of 33% strontium. The RBS channeling of as-grown films showed a minimum channeling parameter of ~4%, indicating excellent epitaxial growth on the SrTiO₃ substrate.

One small sample in each batch was characterized by the physical property measurement system (PPMS) to get the Curie temperature. The T_c was found to be nearly independent of the substrate temperature. The measured magnetic moment as a function of temperature is shown in Figure 1. We see that T_c is close to 360 K. The theoretical maximum for high-quality LSMO is about 370 K.

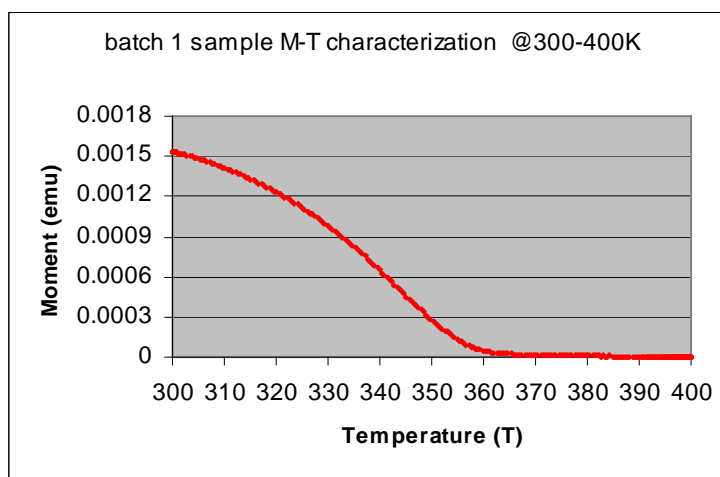


Figure 1: Magnetic properties characterization of one small sample in Batch 1 by PPMS. The Curie temperature is about 360 K. Thickness of this film is around 300 nm.

1.4 Fabrication of Nanotrenches

Our preliminary design required trenches between 50 and 200 nm thick in the LSMO layer. The LSMO on either side of the trench forms the half-metal contact. Initially we explored e-beam lithography with appropriate masking as a means to make narrow trenches. Although e-beam lithography can in principle be used for this purpose, it involves multiple and intricate processing steps. We found a recently developed technique, focused ion beam (FIB) lithography, to be more cost and time efficient in making narrow trenches. We have successfully used FIB lithography to make trenches varying in thickness from ~1 μm (Fig. 2a) to ~25 nm (Fig. 2b). In addition, we observed the trench walls fabricated using FIB to be smooth and clean, a key requirement for enhanced sensor sensitivity.

We made a mask design with 40 devices per 1 cm x 1 cm strontium titanate (STO) substrate. Each device is approximately 200 μm wide. To electrically separate the devices, we etched approximately 50- μm -thick LSMO between the devices. The FIB technique is not appropriate for efficient removal of a large volume of material. We found that Ar-ion plasma etching did not work well and the wet etching with HCl+KI removed the LSMO very quickly and uncontrollably. We finally used accelerated Ar-ion etch and then wire bonded the LSMO contacts. Fully fabricated devices were supplied to Johns Hopkins University for polymer deposition and magnetic testing. In the second round of experiments, SRI deposited similar polymers and conducted electrical testing of the devices.

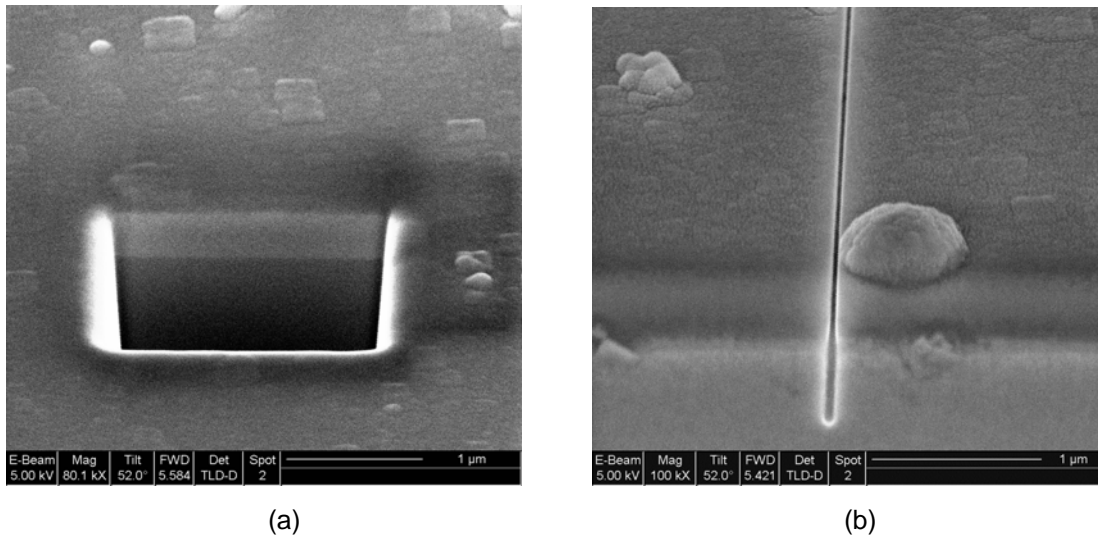


Figure 2: Microtrench (a) and nanotrench (b) made on LSMO with FIB lithography.

1.5 Polymer Synthesis

The polymer synthesis, deposition, and characterization described in this section were carried out at JHU by Professor Howard Katz and coworkers. Calculations carried out at SRI under the DARPA program indicated that polymers with low mobility ($\sim 10^{-5}$ cm^2/Vs) and high carrier density ($\sim 10^{19}$ cm^{-3}) are optimal for enhanced magnetic sensitivity in the proposed spin precession device. In a recent literature report [Majumdar et al., Appl. Phys. Lett. **89**, 122114, 2006], the authors demonstrated spin injection from LSMO into regioregular poly 3-hexylthiophene (P3HT). The mobility and carrier density of this polymer are about 10^{-4} cm^2/Vs and 10^{17} cm^{-3} , respectively. Hence we considered this polymer as a starting point for modifying the characteristics as required for our sensor studies.

The blended polymers are deposited on a Si FET structure to measure the drain current as a function of drain and gate voltages. From the well-known formula for field-effect transistor currents in saturation,

$$I_{D,\text{sat}} = \frac{W}{2L} C_{\text{ox}} \mu_{\text{sat}} (V_G - V_T)^2$$

and the known values of width, length, and capacitance, we obtain the mobility of the polymer.

Then, from measured resistance R and from the following formula we can obtain the free carrier density.

$$R = \frac{1}{nq\mu} \frac{d}{A}$$

n = free carrier density in cm^{-3}

q = 1.6×10^{-19} C

μ = mobility in cm^2/Vs

d = film thickness between source and drain in cm

A = cross-sectional area of the current path in cm^2

R = Resistance in ohm

We carried out two parallel studies. In one study, we systematically blended the insulator polypropylene (PP) into P3HT. Table 1 lists electrical properties obtained from films on Si/SiO₂ with gold electrodes on top and an aspect ratio of the region between electrodes of about 20.

Table 1. Electrical properties of P3HT-polypropylene blends in transistor geometries. Resistance is the two-terminal resistance with zero gate voltage.

	Mobility (cm^2/Vs)	Resistance ($\text{M}\Omega$)	Charge Density ($/\text{cm}^3$)
P3HT only	3.2×10^{-4}	118	1.4×10^{17}
PP 1%	5.3×10^{-4}	31	3.1×10^{17}
PP 2%	6.0×10^{-4}	32	2.7×10^{17}
PP 5%	2.1×10^{-4}	160	1.5×10^{17}
PP 10%	5.1×10^{-4}	66	1.5×10^{17}
PP 25%	0.8×10^{-4}	187	3.4×10^{17}

For low concentrations of PP considered here, neither mobility nor carrier concentration changed systematically. However, as the PP content is increased to 25%, the mobility decreased 4-fold and carrier density increased 2-fold. With more PP, the mobility is expected to decrease even further without affecting the carrier density. Space-charge-limited current measurements in vertical geometries are consistent with these conclusions.

In the other study, we systematically added HBF₄, an acid dopant intended to increase the carrier density. Table 2 lists the results.

Table 2. Electrical properties of P3HT-HBF₄ blends in transistor geometries.

	Mobility (cm ² /Vs)	Resistance (MΩ)	Charge Density (/cm ³)
HBF ₄ 1%	2.4 x 10 ⁻²	4	4.9 x 10 ¹⁶
HBF ₄ 2%	0.6 x 10 ⁻²	65	1.2 x 10 ¹⁶
HBF ₄ 5%	1.7 x 10 ⁻²	9	3.3 x 10 ¹⁶
HBF ₄ 10%	1.9 x 10 ⁻²	4	6.0 x 10 ¹⁶

The measured mobilities are nearly constant and higher than the desired values, and the measured charge densities show no correlation with the dopant concentration. However, by adding PP to the dopant blends, the mobilities are expected to decrease and lower-mobility charge carriers will count toward the charge density. Thus, we expect that an appropriate combination of PP and HBF₄ in P3HT will yield much lower mobility and much higher carrier density than those of bare P3HT. This will be considered in future studies.

We obtained even lower mobilities (than P3HT-HBF₄) with higher charge densities by substituting an organic electron-acceptor dopant, tetrafluorotetracyanoquinodimethane (F4TCNQ). Results are shown in Table 3. A combination with appropriate PP content will be tested in future synthesis.

Table 3. Electrical properties of P3HT-F4TCNQ blends in transistor geometries.

	Mobility (cm ² /Vs)	Resistance (MΩ)	Charge Density (/cm ³)
P3HT only	4.6 x 10 ⁻⁴	18	6.2 x 10 ¹⁷
F4-TCNQ 2%	2.7 x 10 ⁻³	5	3.4 x 10 ¹⁷
F4-TCNQ 5%	3.5 x 10 ⁻³	5	2.6 x 10 ¹⁷
F4-TCNQ 10%	4.3 x 10 ⁻³	4	3.1 x 10 ¹⁷

We attempted to characterize the resistance of P3HT cast between LSMO electrodes, both in nanogaps and between macroscopic electrodes. In the absence of polymers, the device resistance is in gigaohms. With P3HT deposited, there should have been increase in current and decrease in resistance. In one case, deposition between two macroscopic electrodes led to device resistance of ~50 MΩ, convincingly demonstrating a charge injection through polymer. However, when the polymer was deposited on devices with nanotrenches, we did not see any noticeable increase in current.

First we speculated that PP, which is an insulator, got attached to the LSMO walls, thus preventing any charge injection. The device was cleaned with chloroform, which removed all polymers. Then we drop-cast P3HT without PP or HBF₄ on the devices. We did not see any change in current. We then further modified our deposition process to 1) change the solvent from chlorobenzene to chloroform, which has lower boiling point; 2) use a diluted polymer solution (2 mg/mL) for drop-casting; 3) use two kinds of RR-P3HT polymer, one with a molecular weight

of 87,000 from Aldrich and the other with a molecular weight of 70,000 from Rieke Metals, Inc.; 4) deposit polymer under house vacuum before the evaporation of chloroform mother solution; and finally 5) remove the residual solvent by annealing at 85°C for over an hour. In spite of these changes to the deposition methods, we did not see any increased current appropriate for the resistance of the polymer in the nanotrench. We speculated that the polymers, deposited by spin-coat and drop-cast, did not get into the nanotrenches, or that the LSMO electrodes retained an insulating film from their fabrication.

SRI followed up the conclusions from JHU with a local effort to deposit commercially available polymer (P3HT) with a molecular weight of 17,500 and followed the deposition procedure as described above. First, we deposited the polymer in the microgap between the LSMO lines. The side walls were coated with oxide, and the current from LSMO was expected only from the top exposed surface. The current voltage was measured. The resistance calculated for this geometry with the measured values of mobility and carrier concentration matched up very well (mostly within 20%) of the measured resistance. This study confirmed the charge injection through polymer from LSMO. Second, we deposited the polymer in the nanotrench. Our electrical measurements clearly indicated the presence of polymer in the nanotrench. However, the measured current-voltage curve was highly non-ohmic in that the current did not increase linearly with the cross-sectional area or decrease linearly with trench width. This led us to conclude that the charge injection from LSMO to the polymer is through an insulating oxide layer(s). Further literature search revealed that LSMO reacts with Ga-ion to form an insulating and non-ferromagnetic layer [Ono et al., *Appl. Phys. Lett.* **84**, 2370, 2004]. Since the nanotrench was fabricated using the FIB method, which uses a high-energy Ga-ion beam, we infer that an insulating layer created at the surface prevented the charge injection. We concluded that e-beam lithography is required to make the nanotrenches in LSMO. In this approach, an e-beam is used to make an ultra-narrow trench on an e-beam photoresist deposited on LSMO. Then, energetic Ar⁺ ion beam milling (IBM) is used to etch the LSMO away. The important requirement for the e-beam resist is that its IBM etch rate be slower than that of LSMO.

1.6 Noise Modeling

The noise measurement and modeling described in this section were carried out by Professor Nowak at the University of Delaware. In the absence of devices showing both charge and spin injection into the polymer, we focused on characterizing the noise properties of LSMO thin films and regioregular P3HT separately. These studies reveal some of the noise mechanisms relevant to devices and hence provide a rudimentary model for the device noise. Additional noise sources in actual devices may include surfaces of the LSMO sidewalls (due to lithographic processing) and the presence of an interfacial layer between the LSMO sidewall and polymer. We note that noise studies of the polymer were done on macroscopic thin films. The noise of a polymer in the trenches may be different if the width of the trench is smaller than the length scale characterizing the disorder (e.g., grain boundaries) in the polymer film. Next, we describe the noise in patterned LSMO lines and in P3HT that was spin-cast between the gold-coated LSMO contact pads.

SRI patterned LSMO films lithographic-ally into long, narrow lines and post-deposited gold contact pads onto the ends of the LSMO lines. Electrical leads were ultrasonically bonded to the contact pads. The contact resistance of the bonds was ohmic and measured to be less than 3.5Ω per bond pad, far smaller than the LSMO line resistance of $\sim 18 \text{ k}\Omega$. Five LSMO lines (6, 7, 8, 12, and an unknown line) were measured. Both 2-probe and 4-probe techniques were used to measure the resistance, current-voltage characteristics, and noise. The results were indistinguishable, indicating the contacts contributed negligibly to the measured noise power. Figure 3 shows a typical linear I - V characteristic. The resistance of the lines ranges from approximately 17 to 19 $\text{k}\Omega$, which corresponds to an LSMO resistivity of 7 $\text{m}\Omega/\text{cm}$.

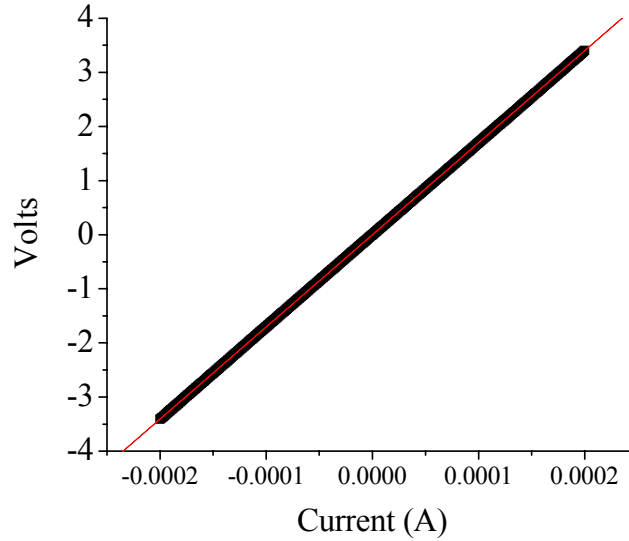


Figure 3: Current-voltage curve for line 12.

Figure 4 shows the voltage noise power spectral density as a function of frequency at different current biases. In this plot the thermal (Johnson) noise of the sample has been subtracted. The measured thermal noise power spectral density was in excellent agreement with the prediction, $4k_BTR$. The spectral dependence shown in Fig. 4 is very close to $1/f$ at low frequencies (below 1 kHz). Also, the noise power is found to scale as the square of the bias current, I , indicating the noise is due to resistance fluctuations in the LSMO material. A Hooge expression can be defined to parameterize the noise:

$$S_v = \alpha \frac{V_{dc}^2}{\Omega f}$$

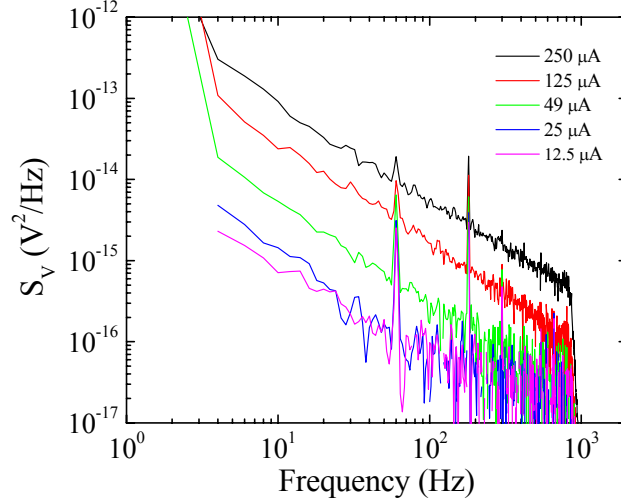


Figure 4: Frequency dependence of the voltage noise power in LSMO line 12 measured for various bias currents. Spikes near 60 and 120 Hz are artifacts associated with 60 Hz power supply lines coupling into the measurement circuit.

In this expression, Ω is the volume of the sample, $V_{dc} = IR$; f is frequency; and the quantity α parameterizes the magnitude of the noise. The quantity α allows comparison of noise on different samples potentially measured under different bias conditions. We note that the inverse scaling with sample volume is plausible but has not been explicitly verified in our samples since they all had the same volume. Of the five LSMO lines measured, for three of them $\alpha = 2 \times 10^{-10} \mu m^3 \pm 1 \times 10^{-10} \mu m^3$, whereas for line 6 $\alpha = 1 \times 10^{-9} \mu m^3$, and for the unknown line gave $\alpha = 1 \times 10^{-8} \mu m^3$. We believe $\alpha = 2 \times 10^{-10} \mu m^3$ is a representative value for LSMO. This value is also consistent with some reports in the literature. Figure 5 shows the magnetoresistance (MR) of LSMO line 12 for the magnetic field applied along the length of the line and perpendicular to the length. The MR is quite small in both cases, being approximately 0.4% for H perpendicular to the line and 0.8% for H parallel to the line.

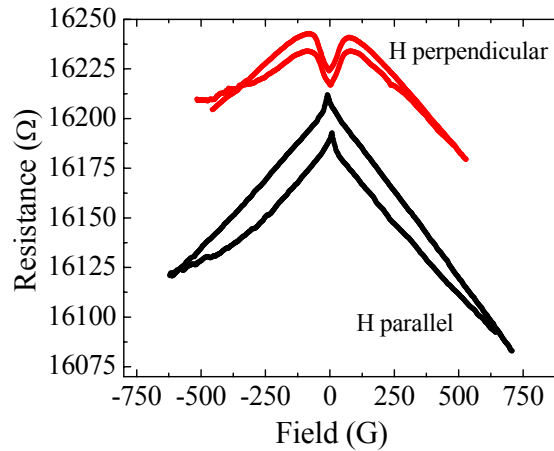


Figure 5: Magnetoresistance of LSMO line 12 for magnetic field applied parallel and perpendicular to the length of the line. Curves offset for clarity.

The magnetic field dependence of the noise power (measured in an octave centered at 11 Hz) is shown in Figure 6. The noise exhibits negligible dependence on magnetic field. In principle, thermal magnetization fluctuations can couple to the resistance (via $(dR/dM)^2$, where M is the magnetization) and generate resistance fluctuations. Under quasi-equilibrium conditions, the signature feature of this magnetic noise is that the resistance noise power varies as dR/dH , the derivative of the magneto-resistance curve in Figure 5. We have not observed this characteristic feature. The most likely reason that $1/f$ magnetic noise is not evident in these LSMO lines is that the magnetoresistance is small. Hence, we attribute the $1/f$ noise in the LSMO as being due to scattering from defects which undergo thermally activated reconfigurations – this is the commonly held explanation for $1/f$ noise in metals.

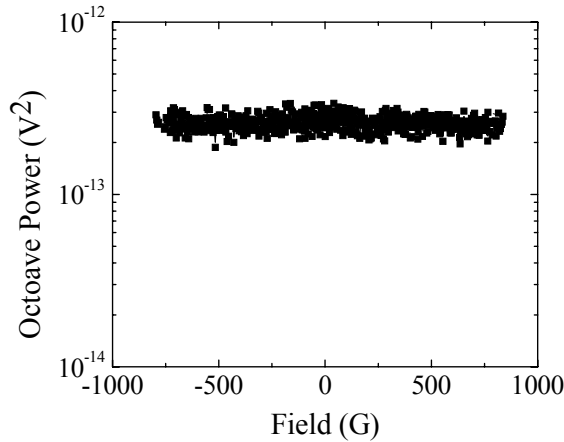


Figure 6: Magnetic field dependence of the noise power measured near 10 Hz for LSMO line 12. Data was taken with a constant current bias of 125 μ A at room temperature.

It is important to note that the following data on P3HT were taken on a different die than the one on which noise in LSMO was measured. The noise in the P3HT polymer was measured in samples that had the polymer either spin-cast or drop-cast across several LSMO lines. In principle, the polymer was confined to a small (but macroscopic) window that was opened up in the SiO_x or SiN_x overlayer that covers the LSMO lines. After examining the polymer under an optical microscope, however, we were concerned that additional polymer, or some unknown residue, had also bridged a number of the contact pads. If so, the current distribution is poorly defined and it is difficult to draw conclusions related to where the noise source(s) are and to establish benchmark parameters for the polymer. Moreover, since LSMO material is used as a contact to the polymer, not all the noise can be simply attributed to the P3HT.

Typical I - V characteristics across different pairs of LSMO having P3HT between them are shown in Figure 7. The curves are nonlinear. The resistance between adjacent LSMO lines (lines 23, 24, 25, 26) is of order $17\text{ M}\Omega$ and scales approximately linearly. That is, $R=16.7\text{ M}\Omega$ between lines 23-24; $R = 32.5\text{M}\Omega$ between 23-25; and $R = 47\text{ M}\Omega$ between 23-26. The data suggest that there is charge injection into P3HT.

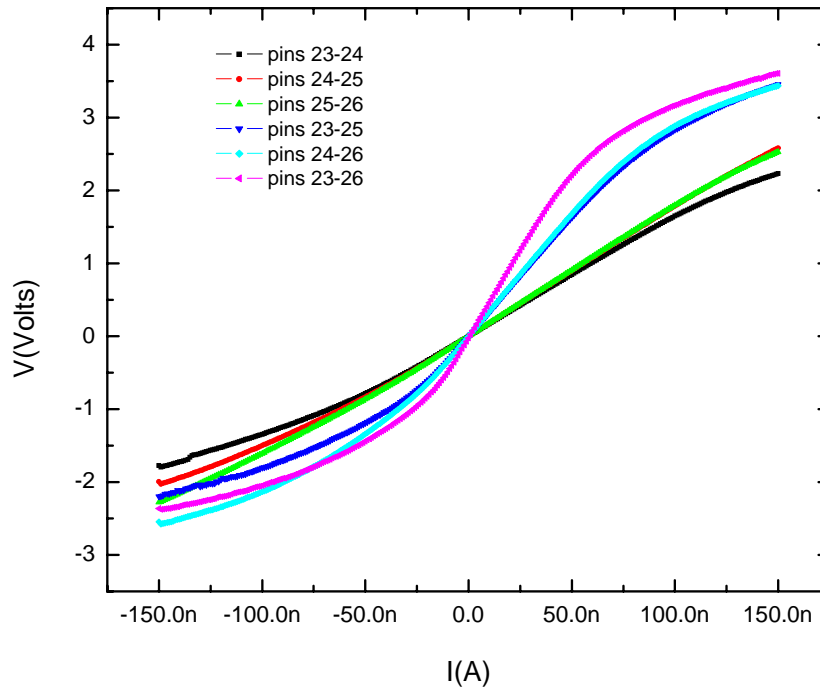


Figure 7: Current-voltage characteristics of P3HT across different LSMO lines.

The noise data we took, however, were not reproducible and showed peculiar, non-monotonic dependence on the bias current (see Figure 8). Noise measurements between some adjacent LSMO lines showed day-to-day variations in noise power as large as a factor of 100. This peculiar behavior is not understood. It is likely that the nonuniform current distribution in the polymer, microstructural aging and unintentional doping from the atmosphere, have a drastic effect on the measured transport properties. Consequently, we draw no conclusions regarding the noise in P3HT at the present time.

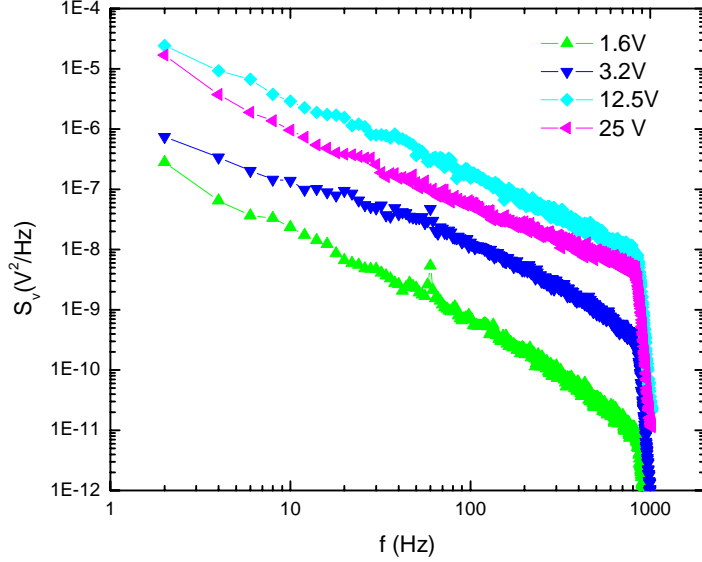


Figure 8: Voltage noise power spectral density in P3HT measured across adjacent LSMO lines 23 and 24.

The final device will consist of a series of two LSMO lines sandwiching a polymer. The voltage noise power in the device can be modeled as the superposition of independent noise sources. At the moment we anticipate that the dominant sources of noise will be thermal Johnson noise related to the equivalent resistance of the entire device, $1/f$ resistance noise in the LSMO, and $1/f$ noise in the polymer. We can safely ignore amplifier noise because the equivalent resistance of the device will be of order $10\text{ M}\Omega$, which yields a thermal Johnson noise level of $400\text{ nV}/\sqrt{\text{Hz}}$, well above the noise level at 1 Hz of a decent differential amplifier. Putting it all together, the voltage noise power spectral density of the device is given by:

$$S_v^{device} = S_v^{Johnson} + S_v^{1/f, LSMO} + S_v^{1/f, P3HT}$$

$$S_v^{device} = 4k_B T R + \alpha \frac{V_{DC, LSMO}^2}{\Omega f} + S_v^{1/f, P3HT}$$

The equivalent magnetic field noise power in teslas per hertz can be computed using the response of the device to magnetic field (dV/dB); namely:

$$S_B^{device} \left[\frac{\text{T}}{\text{Hz}} \right] = \left(\frac{dB}{dV} \right)^2 S_v^{device}$$

Most of the voltage drop across the device will take place across the P3HT, and so the noise contribution from LSMO can be comparatively small. Future work will be directed at quantifying the noise in P3HT in samples having well-defined geometries with uniform current distributions and using low-noise metallic contact pads.

1.7 Improved Spin and Charge Transport Modeling

We had previously considered the electric field inside the organics to be constant and the charge distribution to be homogeneous. In this approximation, the voltage dropped uniformly across the device. This resulted in separate linear differential equations for spin and charge transport. We have improved the calculations to remove those approximations. When the approximations are removed, we find that the required differential equations are nonlinear, as shown below.

$$\nabla \cdot \vec{E} = -\frac{4\pi e}{\epsilon}(\rho_0 - N_D) \quad (1)$$

$$\nabla^2 \rho_0 + \frac{e\vec{E}}{k_B T} \cdot \nabla \rho_0 + \frac{e}{k_B T} \left[-\frac{4\pi e}{\epsilon}(\rho_0 - N_D) \right] \rho_0 = 0 \quad (2)$$

$$\nabla^2 \vec{\rho}^p - \frac{e\vec{E}}{k_B T} \cdot \nabla \vec{\rho}^p + \frac{e}{k_B T} \left[-\frac{4\pi e}{\epsilon}(\rho_0 - N_D) \right] \vec{\rho}^p - \frac{\vec{\rho}^p}{L^2} + \vec{b} \times \vec{\rho}^p = 0 \quad (3)$$

Also notice that the charge transport (Eq. 2) and the spin transport (Eq. 3) have now to be solved self-consistently as they are coupled through the Poisson equation (Eq. 1). We have completed the calculations and found that linear approximation is valid when the organic has a doping density of $6 \times 10^{18} \text{ cm}^{-3}$ or more. For lower dopant densities, the field is far from uniform.

We calculated the response function, dV/dB , the quantity that directly relates to sensitivity. The results are shown in Figure 9 for two dopant concentrations: $6 \times 10^{18} \text{ cm}^{-3}$ (Fig. 9a) and $1 \times 10^{18} \text{ cm}^{-3}$ (Fig. 9b). We see that the previously estimated sensitivity (red line) agrees mostly with the accurately evaluated value (blue line) only at high doping density. This clearly indicates that highly doped organic is needed for enhanced sensitivity.

These calculations and results have been summarized in the form of a manuscript for possible publication in *Physical Review B*. The draft manuscript is enclosed here as Appendix A.

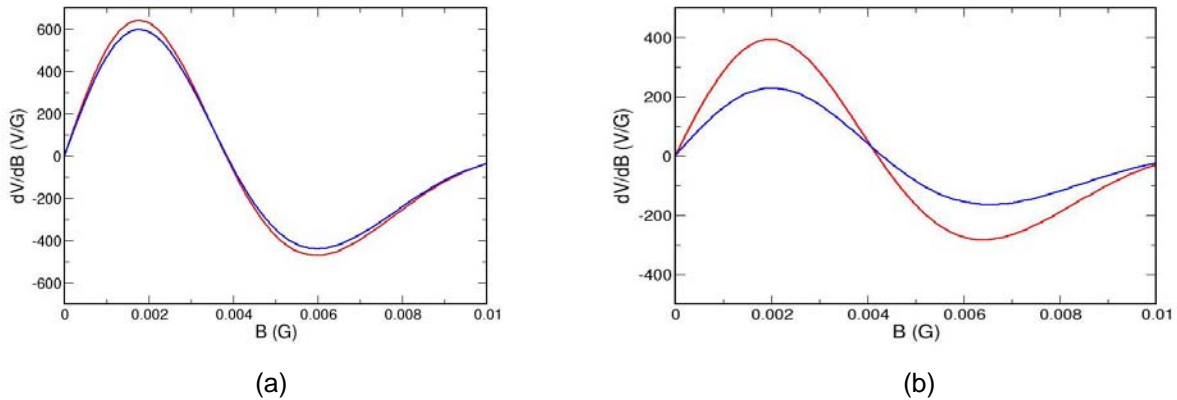


Figure 9: Response function calculated with linear (blue) and nonlinear (red) approximation for dopant density of (a) $6 \times 10^{18} \text{ cm}^{-3}$ and (b) $1 \times 10^{18} \text{ cm}^{-3}$.

1.8 Performance Modeling

The sensitivity of devices is limited by several noise sources related to material properties, device design, interface quality, volume, temperature, concept of operation, instrument, etc. The noise sources fall into four general categories: shot noise, Johnson noise, 1/f noise with magnetic origin, and 1/f noise with nonmagnetic origin. The performance prediction depends critically on the model used to describe each noise. With additional funding to this seedling effort we will develop a database from our measurements for noise modeling. Until then we will use the noise model developed for organics from field-effect transistor (FET) measurements [Martin et al., J. Appl. Phys. **87**, 3381 (2000)] and the spin diffusion length estimated from spin injection experiments [Dediu *et al*, Solid State Comm. **122**, 181 (2002)].

The organics used in these experiments differ from the one we intend to use in our magnetic sensor in three important ways. First, the FET uses crystalline organics with high mobility ($\sim 1 \text{ cm}^2/\text{Vs}$). In our work, we will use low-mobility ($\sim 10^{-5} \text{ cm}^2/\text{Vs}$) organics in amorphous state. The dominant scattering mechanism in crystalline materials need not be the limiting one in the disordered state.

Second, the molecule T_6 used in spin injection experiments contains S atoms. A spin coherence length, L_s , of 50 nm explains their results. We intend to use polymer MEH-PPV in which the heaviest atom is O. Because of the smaller atomic number, the spin-orbit coupling is expected to be weaker and, consequently, the spin coherence time (and length) will be longer in our molecule. An order of magnitude increase in lifetime will increase the coherence length by a factor of $\sqrt{10}$, to about 150 nm.

Third, the work function of MEH-PPV (5.1 eV) is nearly well matched to that of contact LSMO (4.8 eV), and the contact resistance in our device is expected to be much lower. We will revisit these calculations when data on our structures are available. To study the trends, we use two values of L_s and the parameters deduced from FET measurements.

From FET measurements, the 1/f noise current spectral density, S_i , was found to be proportional to i^2/d^2 , where i is the total current and d is the channel thickness. With C_0 as the proportionality constant, we have

$$S_i = \frac{C_0 i^2}{d^2 f} \quad \left[\text{A}^2/\text{Hz} \right] \quad (4)$$

From the measured values of I , d , and S_i , we obtain a value of 10^{-16} cm^2 for C_0 at $f=1 \text{ Hz}$. Then, from the well known and simple relationship, the 1/f noise magnetic spectral density S_H and sensitivity η in $N \times N$ array of sensor can be obtained.

$$\begin{aligned}
S_H &= \frac{S_i}{N^2 i^2} \frac{R^2}{(dR/dH)^2} \\
&= \frac{C_0}{N^2 d^2 f} \frac{R^2}{(dR/dH)^2} \\
&= \frac{C_0}{N^2 d^2 f} \frac{V^2}{(dV/dH)^2} \quad [T^2/Hz] \tag{5}
\end{aligned}$$

$$\begin{aligned}
\eta &= \sqrt{S_H} \\
&= \frac{\sqrt{C_0/f}}{N d} \frac{V}{(dV/dH)} \quad [T/\sqrt{Hz}] \tag{6}
\end{aligned}$$

In our transport modeling work, as described in the previous section, we found that the largest (dV/dB) is possible only when the field is constant in the device. The constant field condition is satisfied when the doping density is at least $5 \times 10^{18} \text{ cm}^{-3}$. In our performance studies reported here, we assumed a doping density of $1 \times 10^{19} \text{ cm}^{-3}$ and used a linear model for transport.

For a chosen value of 1000 nm for d , 10 kV/cm for electric field strength E , we calculate the potential V across the organics and the bias magnetic field at which the (dV/dB) is largest. These values are substituted in Eq. (6) for a 100 x 100 array to obtain sensitivity at 1 Hz as a function of carrier mobility, μ , and plotted for two values of spin coherence lengths as shown in Figure 10.

We see that detectivity (solid lines) improves with spin coherence length and the best value of $\sim 10 \text{ fT}/\sqrt{\text{Hz}}$ is predicted when $\mu \sim 5 \times 10^{-7} \text{ cm}^2/\text{Vs}$ in this sensor array operating at room temperature. Also plotted in Figure 10 is the required power density (dotted lines) in mW/cm^2 . Best sensitivity with very low power consumption ($\sim 5 \text{ mW}/\text{cm}^2$) is possible in these devices.

So far, we have used a value for L_s that is independent of mobility. Since the diffusion constant depends on mobility, it is possible that L_s is proportional to $\sqrt{\mu}$. Under this assumption, the calculations are repeated and results are displayed in Figure 11. At very low mobilities, the spin coherence length decreases and, consequently, the detectivity performance deteriorates. The minimum in detectivity is $\sim 50 \text{ fT}/\sqrt{\text{Hz}}$, but at a slightly higher mobility ($\sim 10^{-5} \text{ cm}^2/\text{Vs}$). The required higher mobility results in lower resistance and higher current. Correspondingly, the required power density also increases to nearly $100 \text{ mW}/\text{cm}^2$.

The effects of the electric field and doping density are shown in Figure 12a. With the smaller reduction in E to 8 KV/cm (blue lines), the power density gets smaller. However, the sensitivity performance gets correspondingly worse. Similarly, by decreasing the dopant density from 10^{19} cm^{-3} to 10^{18} cm^{-3} , the conductivity decreases and hence the power density also decreases. Note that the sensitivity performance gets worse by a factor of 2. Finally, we carried out studies to evaluate the thickness dependence. The results are shown in Figure 12b.

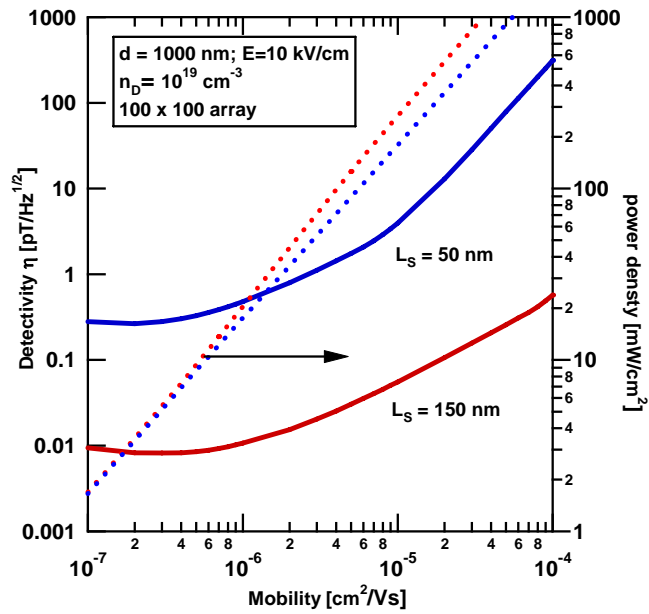


Figure 10: Predicted variation of detectivity and power density with mobility and spin coherence length.

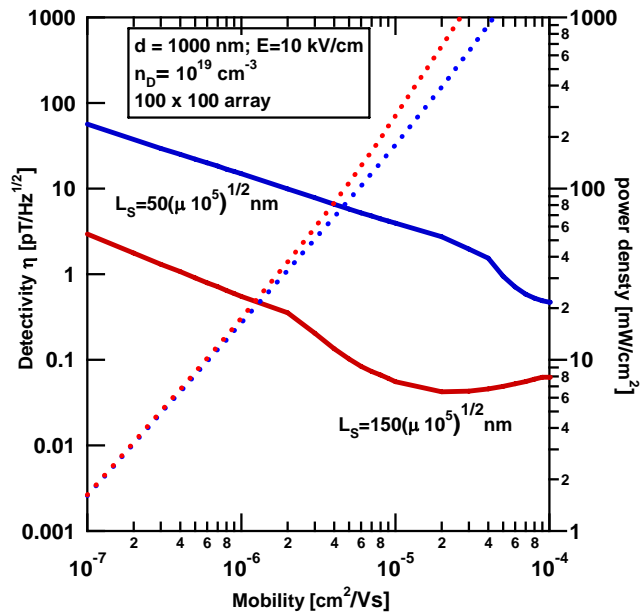


Figure 11: Predicted variation of detectivity and power density with mobility and modified spin coherence length.

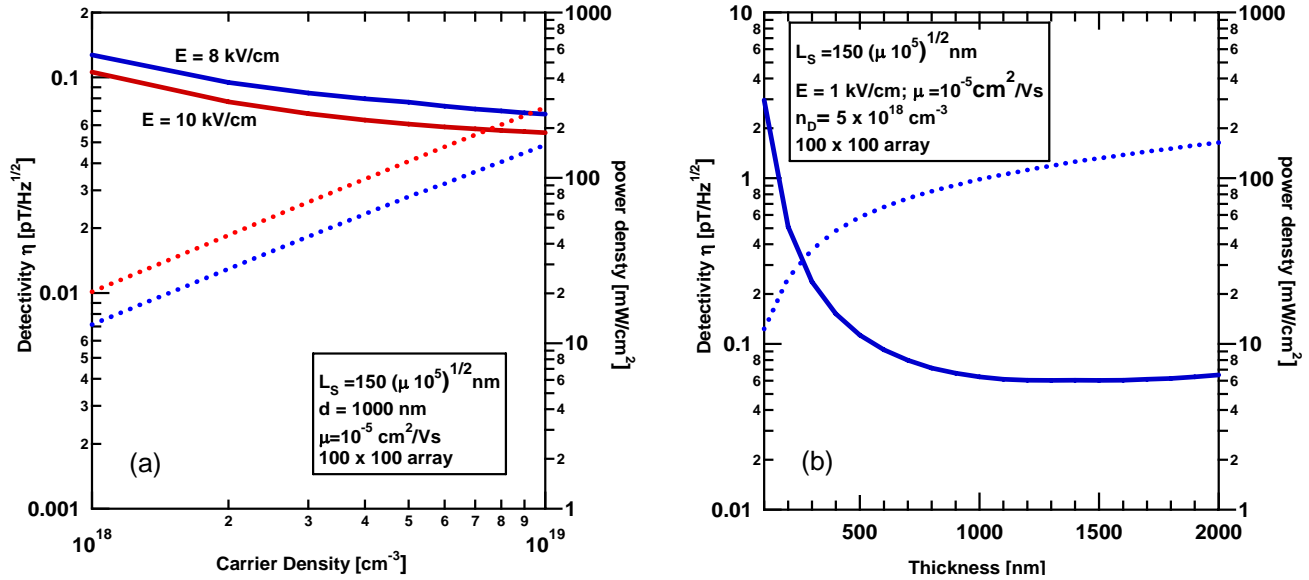


Figure 12: Predicted variation of detectivity and power density with electric field, dopant density (a) and device thickness (b). The assumed parameters are shown in the legend.

When the thickness is much smaller than the spin diffusion length, we do not take full advantage of long transit times required for enhanced performance. As the thickness is increased, we have more time to manipulate the electron spin and the detectivity improves. Beyond some threshold value of thickness, the detectivity saturates at about 60 fT/ $\sqrt{\text{Hz}}$. Since the increase in length also causes the resistance to increase, the power density increases as shown. If the thickness is larger than the spin diffusion length, both detectivity and power dissipation will be worse.

A clarification about the power density is in order. Although the calculated power density values appear to be large (~ 100 mW/cm²), this heat is generated only across the organic whose cross-sectional area is $200 \mu\text{m} \times 0.3 \mu\text{m}$. So, total power used by a 100×100 array is $(100 \times 10^{-3} \times 200 \times 0.3 \times 10^{-8} \times 10^4)$ W. Since this array is expected to be placed on $2.5 \text{ cm} \times 2.5 \text{ cm}$ substrates, the fully normalized power density is only $96 \mu\text{W}/\text{cm}^2$.

1.9 Conclusions

The sensitivity and power density values depend intricately on the device thickness, spin coherence length, mobility, electric field, dopant density, and bias magnetic field. Although it is difficult to arrive at optimum values for all these parameters without a noise model appropriate to our polymer and device design, we can observe the following requirements.

- The surface roughness of the LSMO layer needs to be improved. The preferred target level for the boulder density is $\sim 10^4$ per cm². Since we plan to have 10^4 devices on 1 in. x 1 in. substrate, we would on the average have one boulder per LSMO contact.
- With improved growth quality of LSMO, the T_c is expected to slightly increase from the current value of 360 K. The theoretical maximum is 370 K.

- Currently LSMO is grown on SrTiO₃ substrates, which are commercially available only in 1 cm x 1 cm. However, for eventual fabrication of a 100 x 100 array on a 1 in. x 1 in. area, LSMO growth on large area substrates must be explored.
- The work function of LSMO is known to vary from 4.8 eV. We require organic materials whose HOMO level (for hole devices) or LUMO level (for electron devices) is located near 5.1 eV. This will reduce the contact resistance and enable efficient charge injection. The HOMO level value available in the literature for MEH-PPV is 5.1 eV (i.e., 0.3 eV barrier for holes). With appropriate treatment of the interface, this barrier could be overcome.
- The exact value of the required mobility will depend on the noise model developed, but it appears that mobilities in the range 5×10^{-7} to 5×10^{-5} cm²/Vs will be required.
- Appropriate approaches to reduce the contact barrier (by about 0.5 eV) and improve ohmic contact must be explored. For example, interface dipoles can be exploited.
- The organic must be truly disordered and amorphous in form. Appropriate treatment to either remove the defects or bury their levels deep in the band gap must be explored. Charged impurity scattering and low-lying defect levels contribute to noise.
- The n-doping density in the organic must be at least 5×10^{18} cm⁻³, and preferably 10^{19} cm⁻³. The electric field does not appear to be an issue, because dielectric breakdown of most organics occurs at $\sim 5 \times 10^6$ V/cm, and our device must operate in the $\sim 10^4$ V/cm range.
- Although the FIB method is successful in making required nanotrenches, the use of Ga⁺ ion negates the purpose by coating the LSMO surface with oxide. The spin and charge injections are severely affected.
- The e-beam lithography with Ar⁺ ion milling should be used for making nanotrenches.
- Signal analysis techniques for an efficient on-chip integration of 100 x 100 array signal must be developed.
- Since the response function takes its maximum value at very low bias magnetic fields ($\sim \mu\text{G}$ to mG), this array of devices will most likely be operated on a feedback loop control mode. Explicitly, an external constant current circuit will provide the required optimum bias field in the organics. When the signal magnetic field is detected, the current in the circuit will change and the external circuit will adjust the current to compensate this change. The signal is deduced from the correction applied by the external circuit.

2. FIELD EFFECT TRANSISTOR

Both the magnetic sensor and the magnetic-field-effect transistor have a common LSMO-polymer-LSMO structure. Once a metal and a semiconductor are brought into close contact, a Schottky barrier, as well as a depletion layer, will be formed at the interface, which can significantly modify charge transport and electric-field distribution inside a device. Since our device's operation sensitively depends on the interplay of the transit and precession times, it is important to examine the robustness of the performance predicted with simplified models.

We have developed a complete device model, where both the Schottky-barrier effect and the electric-field-dependent carrier mobility are taken into account. We have considered both the thermionic-emission and the tunneling currents and solved charge and spin transport equations self-consistently. This model provides a realistic and accurate description of spin-dependent transport in the organic spin devices.

2.1 Schottky Barrier

The Schottky barrier height in a metal-semiconductor junction is

$$\phi_{\text{Bn}} = \phi_m - \chi$$

where $e\phi_m$ is the metal work function, and $e\chi$ is the electron affinity measured from the bottom of the conduction band. Due to the image force, the Schottky barrier is lowered,

$$\tilde{\phi}_m = \phi_m - \sqrt{\frac{eE(0)}{4\pi\epsilon}}$$

where $E(0)$ is the field at the boundary and the barrier reduction only occurs when the direction of $E(0)$ is pointing from the metal to the semiconductor. The current across a barrier consists of a contribution from thermionic emission and electron tunneling, which leads to a spin-dependent interfacial conductance. The up-spin conductance is

$$G_{\uparrow}^* = A^* T^2 \frac{e}{k_B T} \left[\exp\left(-\frac{e\tilde{\phi}_{\text{Bn}}}{k_B T}\right) + \exp\left(-\frac{e\phi_{\text{Bn}}}{E_{00}}\right) \right],$$

where the first term is from the thermionic-emission and the second is from the tunneling. The Richardson constant A^* is given by

$$A^* = \frac{4\pi e m^* k^2}{h^3},$$

where m^* is the electron effective mass of the polymer and

$$E_{00} = \frac{e\hbar}{2} \sqrt{\frac{N_D}{em^*}}$$

measures the effectiveness of tunneling, which depends on both the doping concentration N_D and m^* . The total conductance at the LSMO-polymer interface is then

$$G_{\uparrow} = \left(1/G_{\uparrow}^* + 1/G_{\uparrow}^0\right)^{-1},$$

where G_{\uparrow}^0 is the up-spin conductance in the absence of the Schottky barrier. The conductance for different spins are related by $G_{\downarrow}/G_{\uparrow} = G_{\downarrow}^0/G_{\uparrow}^0$ and $G_{\uparrow\downarrow}/G_{\uparrow} = G_{\uparrow\downarrow}^0/G_{\uparrow}^0$. The carrier density at the boundary between the metal and the semiconductor is

$$\rho_0(0) = N_c \exp\left(-\frac{e\tilde{\phi}_{\text{Bn}}}{k_B T}\right),$$

where N_c is the effective density of state in the semiconductor, which is proportional to $(m^*)^{3/2}$. m^* in a polymer is usually larger than in an inorganic semiconductor, such as Si.

2.2 Electric-Field Dependent Mobility

Carrier mobilities in polymers often strongly depend on the electric field and are found to obey the Poole-Frenkel relation,

$$v = v_0 \exp\left(\sqrt{\frac{E}{E_c}}\right),$$

where v is the mobility and E_c measures how strong the field-dependence is. This Poole-Frenkel behavior originates from the disorders (traps) in the polymer. In a polymer with many carriers, as in these organic spin devices, the deep traps will likely be filled by the carriers, and the field-dependence is not as strong as in undoped or very lightly doped polymers.

2.3 Transport Equations

The field-dependent carrier mobility will introduce a few new terms in the charge-spin transport equations. We solve the following equations

$$\begin{aligned} \frac{d^2 \rho_0}{dx^2} + \frac{d\rho_0}{dx} \left(\frac{eE}{k_B T} + \frac{1}{v} \frac{dv}{dE} \frac{dE}{dx} \right) + \frac{e\rho_0}{k_B T} \left(\frac{dE}{dx} + \frac{E}{v} \frac{dv}{dE} \frac{dE}{dx} \right) &= 0 \\ \frac{d^2 \vec{f}}{dx^2} + \frac{d\vec{f}}{dx} \left(\frac{eE}{k_B T} + \frac{1}{v} \frac{dv}{dE} \frac{dE}{dx} \right) + 2 \frac{d \ln(\rho_0)}{dx} \frac{d\vec{f}}{dx} + \hbar \times \vec{f} - \frac{\vec{f}}{L^2} &= 0 \\ \frac{dE}{dx} &= -\frac{4\pi e}{\epsilon} (\rho_0 - N_D) \end{aligned}$$

where $\vec{f} = \vec{p} / (e\rho_0/k_B T)$. Here both the spin diffusion length $L \equiv \sqrt{D\tau}$ as well as the effective magnetic field $h \equiv g\mu_B B / D\hbar$ depend on the electric field, via the Einstein's relation between the mobility and the diffusion constant, and consequently are inhomogeneous across the polymer. The Schottky effects are reflected in the boundary conditions, as described earlier. We have developed an efficient and reliable code to numerically solve these equations self-consistently.

2.4 Results

We choose parameters pertinent to a realistic device structure. N_c is 10^{21} cm^{-3} , which is considerably higher than in Si ($3.8 \times 10^{19} \text{ cm}^{-3}$). The corresponding carrier effective mass of the polymer is $m^* = 3.55 m_0$, where m_0 is the bare electron mass. The Schottky barrier of 0.25 V is assumed. This is a typical energy difference between work functions of LSMO and MEH-PPV. A high barrier would not allow even a decent charge injection.

Figure 13 illustrates the electric-field and carrier-density distributions of a LSMO-polymer-LSMO device. With a value of E_c set 10^{10} V/cm, the mobility is essentially independent of the field. We see that a depletion layer is formed at both interfaces and that the electric field in the depletion layers significantly deviates from the value in the middle of the device. Note that the two depletion layers are not symmetric because in the sandwiched structure considered here, one Schottky barrier is under a forward bias and the other is under a reverse bias.

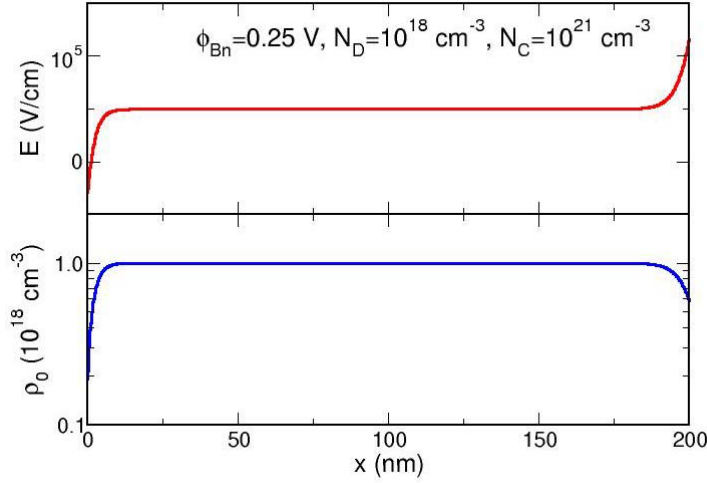


Figure 13: Spatial distributions of electric field (upper panel) and carrier density (lower panel) for an LSMO-polymer-LSMO device structure. The Schottky barrier height is 0.25 V and the doping in the polymer is 10^{18} cm^{-3} .

We plot in Figure 14 the device sensitivity dV/dB for different doping concentrations N_D . For a chosen barrier height of 0.25 V, we see that the dV/dB value obtained in $N_D=10^{18}$ cm^{-3} case is larger than that obtained in the case of either $N_D=10^{17}$ or 10^{19} cm^{-3} . Since the average electric field as well as other parameters is fixed in these calculations for these doping levels, a larger dV/dB value indicates a higher spin injection efficiency from LSMO into the polymer. For a slightly different barrier height of 0.3 V, note from Figure 15 that the dV/dB value is larger for $N_D=10^{17}$ cm^{-3} than for $N_D=10^{18}$ or 10^{19} cm^{-3} .

We plot in Figure 14 the device sensitivity dV/dB for different doping concentrations N_D . For a chosen barrier height of 0.25 V, we see that the dV/dB value obtained in $N_D=10^{18}$ cm^{-3} case is larger than that obtained in the case of either $N_D=10^{17}$ or 10^{19} cm^{-3} . Since the average electric field as well as other parameters is fixed in these calculations for these doping levels, a larger dV/dB value indicates a higher spin injection efficiency from LSMO into the polymer. For a slightly different barrier height of 0.3 V, note from Figure 15 that the dV/dB value is larger for $N_D=10^{17}$ cm^{-3} than for $N_D=10^{18}$ or 10^{19} cm^{-3} .

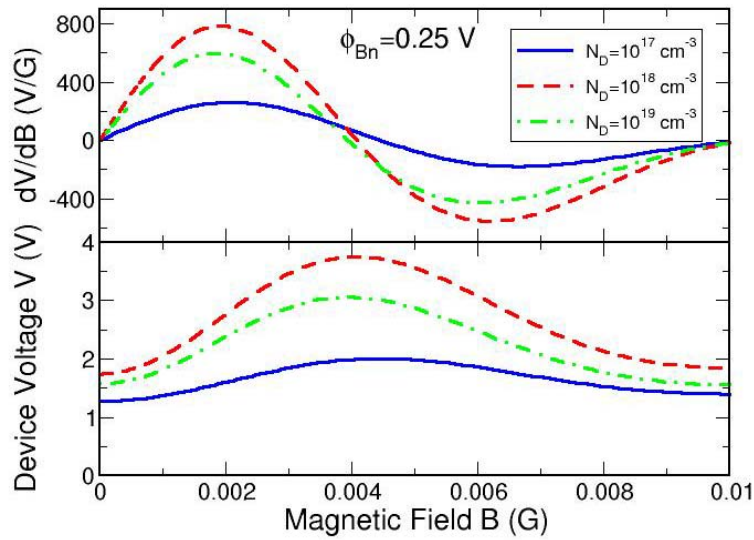


Figure 14. Device sensitivity dV/dB (upper panel) and device voltage V (lower panel) as a function of an applied magnetic field for different doping concentrations. Constant current and electric field ($\sim 5 \times 10^4 \text{ V/cm}$) are assumed. The barrier height is 0.25 V.

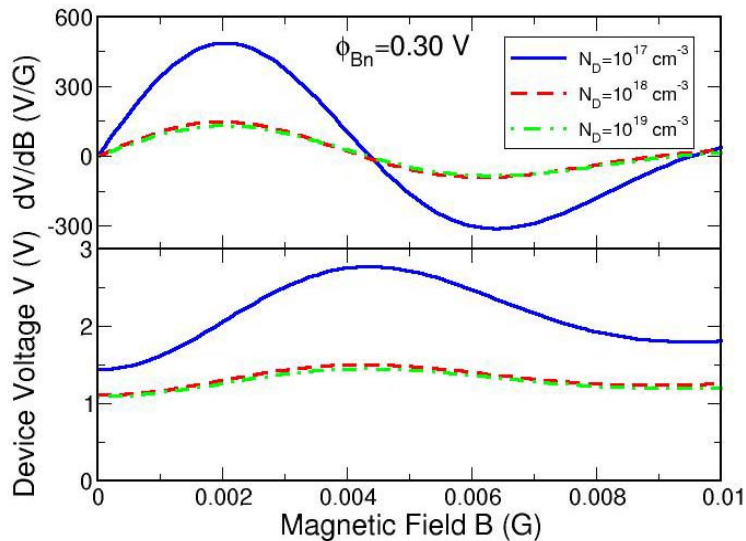


Figure 15. Device sensitivity dV/dB (upper panel) and device voltage V (lower panel) as a function of applied magnetic field for different doping concentrations. The barrier height is 0.3 V. Other parameters are the same as in Fig. 14.

As N_D increases, the Fermi level in the polymer moves closer to the conduction band edge. The effective barrier height increases and consequently the thermionic-emission current is reduced while the tunneling current is enhanced, which modifies dV/dB . Thus the above results indicate that spin injection can be enhanced by engineering Schottky barrier properties such as the barrier height and the doping in the semiconductor.

Figure 16 compares results with different N_C for a barrier height of 0.25 V. The values dV/dB for $N_C = 5 \times 10^{21}$ and 10^{21} cm^{-3} are similar, but are quite different from those for $N_C = 2 \times 10^{20} \text{ cm}^{-3}$. A smaller N_C means a smaller carrier effective mass, which would result in a larger tunneling current. The reduced dV/dB for $N_C = 2 \times 10^{20} \text{ cm}^{-3}$ suggests that when effective electron tunneling (smaller effective mass) is larger, the spin injection is reduced.

We describe the effect of the field-dependent mobility on the device performance in Figure 17. We see that this effect becomes notable only when E_c is 10^5 V/cm , and even then dV/dB is not significantly affected. $E_c = 10^5 \text{ V/cm}$ is a typical value for undoped polymers and denotes a very strong electric-field dependence of the mobility. It appears that field dependence in the cases of doped polymers will not play a significant role. The weak effect of field-dependent mobility on the device performance is possibly because the electric field is largely homogeneous inside the device, except in the depletion layers.

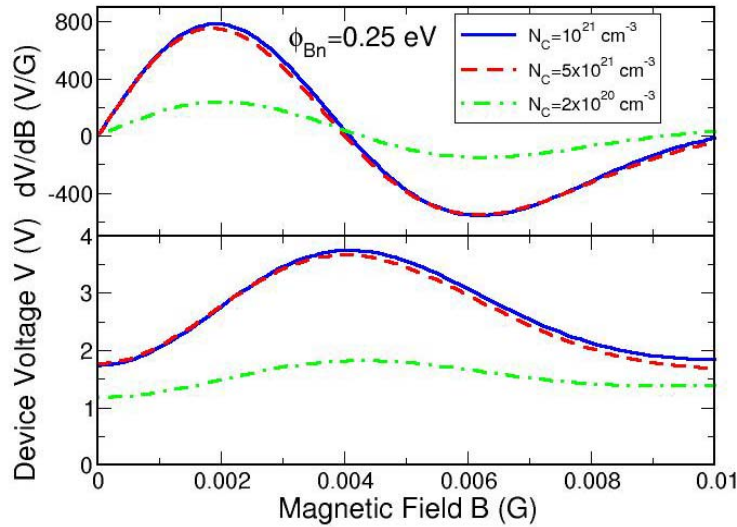


Figure 16: Device sensitivity dV/dB (upper panel) and device voltage V (lower panel) as a function of applied magnetic field for values of N_C . The barrier height is 0.25 V. Other parameters are the same as in Figure 8.

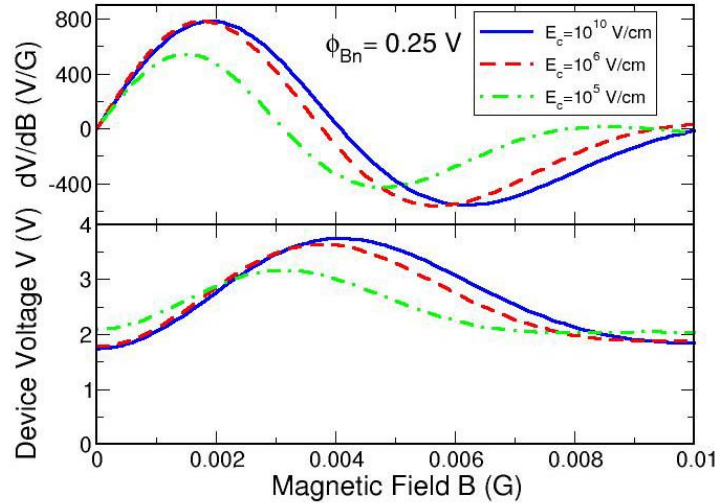


Figure 17: Device sensitivity dV/dB (upper panel) and device voltage V (lower panel) as a function of applied magnetic field for different E_c , which measures how sensitive the mobility depends on the field. The barrier height is 0.25 V. Other parameters are the same as in Figure 14.

In conclusion, our results, which are based on the realistic and accurate modeling that includes Schottky barrier effects as well as field dependence of the mobility, have demonstrated the robustness of the performance predicted from a simplified model. This model also suggests new degrees of freedom, such as the barrier height, carrier effective mass, and doping concentrations, to be engineered to achieve high performance of organic spin devices.

3. LIGHT PROPAGATION IN GaAs

SRI had previously developed codes to study high-intensity light propagation through semiconductor compounds and alloys. The codes are now extended to the short-wavelength region and applied to GaAs. The required propagation parameters, including intrinsic carrier density, one-photon absorption coefficient (α), two-photon absorption coefficient (β), free carrier absorption coefficient (σ), and refractive index changes arising from carrier density and temperature, are calculated from full band structures. The excellent comparison between the calculated and the measured α (as seen in Figure 18) indicates that both band structures and dipole matrix element calculations are accurate. The calculated values of β are small, of the order of 10 cm/GW, and decrease with the wavelength (Figure 19).

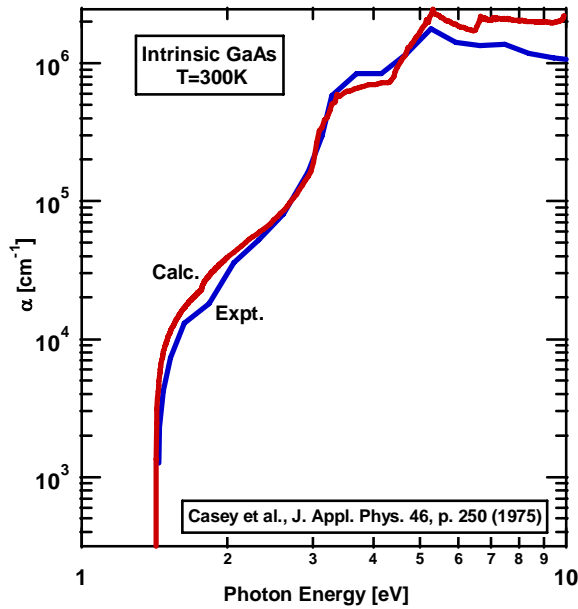


Figure 18: One-photon absorption in GaAs

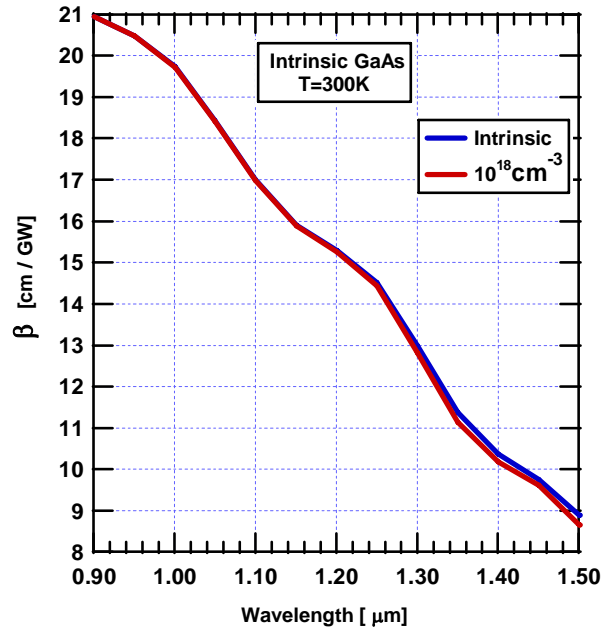


Figure 19: Two-photon absorption in GaAs

Due to the absence of free carrier absorption by holes in the wavelength region of 1 μm to 2 μm , the calculated σ is extremely small (of the order of 10^{-20} cm^2). However, the cross section increases with wavelength and temperature (shown in steps of 50 K in Figure 20). The calculated values of α , β , σ are used in a Kramer-Kronig relationship to obtain the change in refractive index. We find that the index changes linearly with the carrier density (Figure 21) with a slope of -2×10^{-21} . The calculated refractive index increases with T at a rate of about 10^{-4} per K.

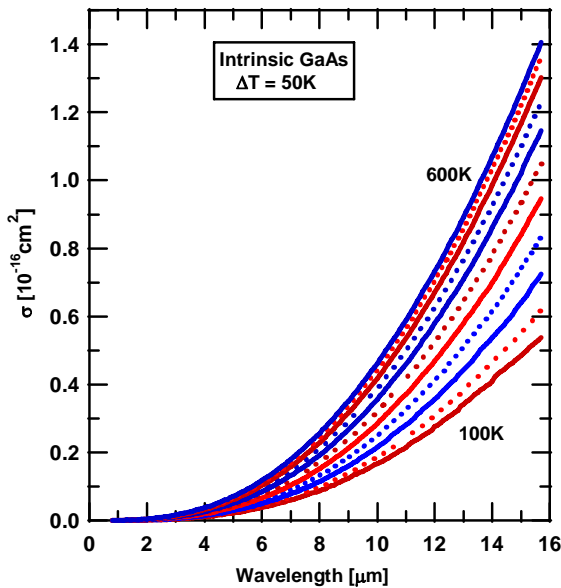


Figure 20: Free carrier absorption in GaAs

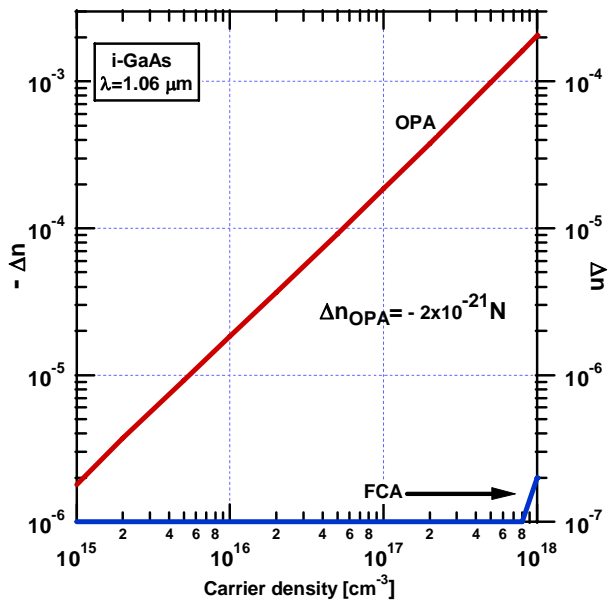


Figure 21: Index change with carrier density in GaAs

These calculated values are then used in our three-dimensional light propagation code to obtain the output intensity as a function of input intensity. This code considers both absorption and refraction in the material on numerical mesh and solves the time-dependent Maxwell's equations as a function of distance. The calculated limiting of the light with a wavelength of $1.06 \mu\text{m}$ is shown in Figure 22 (solid line); the measured values [Boggess et al., IEEE J. Quan. Elec. **21**, 488 (1985)] are shown as filled circles. We see that the trend is predicted accurately and the calculated values are within experimental accuracy. If the β value of 22 cm/GW is used instead of 18 cm/GW , we see (dashed line) an excellent numerical agreement as well.

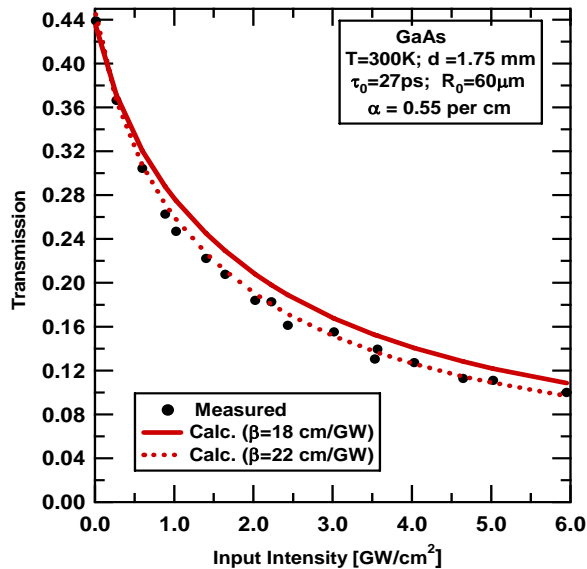


Figure 22: Optical limiting in GaAs.

The codes can now be used to study $1.5 \mu\text{m}$ light propagation through organic molecules and polymers with the values of β and σ measured under DARPA's MORPH program. In the next period, we will evaluate the nonlinear absorption parameters required for the optical limiting goals of the MORPH program. We have further applied our codes to study light propagation through GaInAs and GaAsP alloys and concluded that GaAsP alloys are better than either GaAs or GaInAs alloys for limiting $1.5 \mu\text{m}$. The results are summarized for possible publication in *Applied Physics Letters*. The draft manuscript is enclosed here as Appendix B.

Appendix A

Self-consistent spin-charge transport in organic device structures

Z. G. Yu

*Physical Sciences Division, SRI International, 333 Ravenswood Avenue, Menlo Park, California 94025, USA**

(Dated: April 1, 2008)

We present a comprehensive model to describe spin transport across an organic material sandwiched between magnetic contacts. We solve a set of differential equations for transport of charge and spin, together with the Poisson equation. Both the electric-field-induced spin and charge drift and the magnetic-field-induced spin precession are included. We also consider the effects of a Schottky barrier between the metal contact and organic materials and of electric-field dependent carrier mobility. The magnet-polymer-magnet structures were proposed to achieve ultrasensitive magnetometers and low-power magnetic-field-effect transistors because a weak magnetic field can significantly modify spin transport through spin precession. The numerical results based on the comprehensive modeling suggest that the organic device structures that exploit low carrier mobility and long spin lifetimes for magnetic-sensing and magnetic-field-effect transistors are robust.

PACS numbers:

I. INTRODUCTION

In spin-based electronics (spintronics), information is carried by the electron spin. Because of the nature of magnetic interactions between electron spins, spintronic devices have the potential advantages of non-volatility, increased data processing speed, and decreased electric power consumption. Inorganic semiconductor spintronic devices have attracted considerable attention¹ since the discovery of long spin lifetimes in semiconductor structures². Injection, manipulation, and detection of spin polarization in semiconductors have been extensively investigated both experimentally and theoretically.

Compared with inorganic materials, organics have much longer spin lifetimes because of the vanishing spin-orbit couplings, suggesting that organic materials have significant potential for novel spintronic devices. Recently, strong magnetoresistances and large spin injection have been observed in $\text{La}_{0.7}\text{Sr}_{0.3}\text{MnO}_3$ (LSMO)/sexithienyl (T_6)/LSMO and LSMO/8-hydroxyquinolate aluminum (Alq_3)/Co structures even at room temperature^{3,4}. T_6 and Alq_3 are two widely used materials in organic electronics like light-emitting diodes. Theoretical studies of spin-dependent transport in magnet-polymer-magnet structures have just begun. A systematic theoretical study of spin injection, spin manipulation, and spin detection in organic structures is required to understand the experiments and to design new organic spintronic devices.

Organic electronic devices, including light-emitting diodes and field-effect transistors, have been the subjects of intense research in the last decade because they have processing and performance advantages for low-cost and/or large-area applications⁵. On the other hand, the low carrier mobility ($10^{-8} - 10 \text{ cm}^2/\text{Vs}$) in organics limits their application for high-speed devices such as computer processors. The arena of organic electronic devices is in the applications that exploit unique properties in organics, such as large-area processing, mechanical flexibility, tunable light emission, chemical sensing interactions,

and biocompatibility. Similarly, organic spintronic devices have some unique applications that are inaccessible to inorganic spintronic devices.

Recently a spin drift-diffusion-precession equation was derived to explain experiments and design organic spin devices⁶. It was found that the low carrier mobility and the long spin lifetime in organic materials provide an ideal condition to exploit the interplay of electric-field-induced spin drift and magnetic-field-induced spin precession to make ultrasensitive magnetic sensors and low-energy magnetic-field-effect transistors. Very recently, spin precession and the resulting oscillatory resistance were successfully observed in the spin-drift regime⁷ in Si ⁸. In Ref. 6, to capture major physics, a few approximations that assume a uniform electric field across the device structure and a carrier mobility independent of electric field were adopted. These approximations allow one to obtain separate linear differential equations for spin and charge transport, which are relatively easy to solve. In general, however, the electric field is inhomogeneous, particularly near the contacts in organic device structures. In addition, carrier mobility in organic materials may strongly depend on electric field and carrier density. Moreover, there exists a Schottky barrier between the metal contact and the organic material. Since the devices operation exploits the interplay of the transit and precession times, it is important to examine the robustness of the performance predicted with simplified models. The comprehensive model also provides a designing tool for organic spintronic devices.

In this work we go beyond the approximations and provide a complete description of spin-dependent transport in magnet-polymer-magnet structures. To make the theory general enough to cover most structures, we include both electric-field-induced spin drift and magnetic-field-induced precession and the magnetization of the two magnets can be noncollinear. The comprehensive model also provides a designing tool for organic spintronic devices. We assume spin-dependent transport across organic structures is diffusive rather than tunneling. The

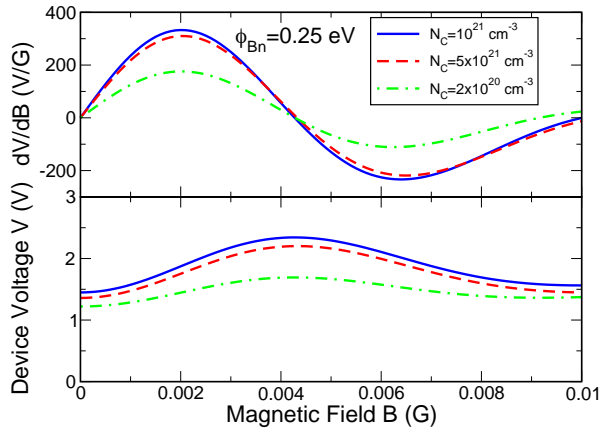


FIG. 1: Spatial distributions of electric field (upper panel) and carrier density (lower panel) for an LSMO-polymer-LSMO device structure. The Schottky barrier height is 0.25 V and the doping in the polymer is 10^{18} cm^{-3} .

paper is organized as follows. In Sec. II, a complete set of drift-diffusion-precession equations are presented. In Sec. III, we analyze the effects of the Schottky barrier and the field-dependent mobility. We present numerical results in Sec. IV, and Sec. V summarizes our results.

II. SPIN CHARGE DRIFT-DIFFUSION-PRECESSION EQUATIONS

When a voltage is applied to a magnet-polymer-magnet structure, a spin-polarized current is injected into the polymer from the magnets, giving rise to spin accumulation in the polymer. To consider spin precession and noncollinear configurations, where spin accumulation can be along any direction, we use a 2×2 density matrix in spin space to describe the carrier distribution, $\hat{\rho}^P = \rho_0^P \hat{\mathbf{1}} + \hat{\boldsymbol{\sigma}} \cdot \boldsymbol{\rho}^P$. Here $\rho_0^P \hat{\mathbf{1}}$ is the equilibrium carrier distribution of the nonmagnetic polymer, and $\hat{\boldsymbol{\sigma}} = (\hat{\sigma}_x, \hat{\sigma}_y, \hat{\sigma}_z)$ are Pauli matrices. In the previous work, to emphasize the spin-dependent part in carrier transport, as a simplification, we assume that the charge distribution inside the polymer is homogeneous, and $\nabla \rho_0^P = 0$ and $\nabla \cdot \mathbf{E} = 0$, and in the steady state we obtain

$$\nabla^2 \boldsymbol{\rho}^P - \frac{e\mathbf{E}}{k_B T} \cdot \nabla \boldsymbol{\rho}^P - \frac{\boldsymbol{\rho}^P}{L^2} - \mathbf{b} \times \boldsymbol{\rho}^P = 0, \quad (1)$$

where $\mathbf{b} \equiv g\mu_B \mathbf{B} / \hbar D$ and $L = \sqrt{D\tau_S}$. This equation provides a simple description of spin drift and spin precession in polymers.

In general, however, the local electric field and the charge distribution are interdependent, an accurate description requires self-consistently solving Poisson's equation together with transport equations. To this end, we start from the general form of a spin-polarized current in the organic material, which consists of two contributions,

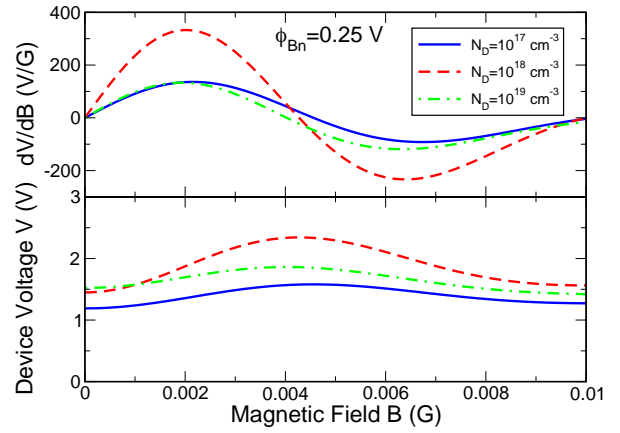


FIG. 2: Device sensitivity dV/dB (upper panel) and device voltage V (lower panel) as a function of an applied magnetic field for different doping concentrations. Constant current and electric field ($\sim 5 \times 10^4 \text{ V/cm}$) are assumed. The barrier height is 0.25 V.

drift and diffusion,

$$\hat{\mathbf{j}}^P = \hat{\rho}^P e \nu \mathbf{E} - e D \nabla \hat{\rho}^P, \quad (2)$$

where ν is the carrier mobility and D the diffusion constant in the organic material. Here we neglect the possible magnetic-field effect on the orbital motion (Hall effect), which is reasonable in polymers with low carrier mobilities. In a nondegenerate system, ν and D are connected via Einstein's relation $\nu / eD = 1 / k_B T$. The continuity equation for each component of the density matrix in the presence of a magnetic field, B , reads

$$\frac{\partial \hat{\rho}^P}{\partial t} = -\frac{\hat{\rho}^P - \rho_0^P \hat{\mathbf{1}}}{\tau_S} - \frac{1}{e} \nabla \cdot \hat{\mathbf{j}}^P + \frac{i}{\hbar} \left[\hat{\rho}^P, -\frac{g\mu_B}{2} (\hat{\boldsymbol{\sigma}} \cdot \mathbf{B}) \right], \quad (3)$$

The above transport equations need to be solved together with the Poisson equation,

$$\nabla \cdot \mathbf{E} = -\frac{4\pi e}{\epsilon} (\rho_0 - N_D) \quad (4)$$

where N_D is the ionized donor density. The inclusion of the Poisson equation in the spin transport theory makes an exact solution impossible, and we have to resort to numerical integration of these coupled differential equations. Suppose the electric field is along the x -axis and spin and charge distributions are uniform along $y-z$ plane, the spin-charge drift-diffusion equations in the steady state ($\frac{\partial \hat{\rho}^P}{\partial t} = 0$) can be written as

$$\frac{d^2 \rho_0}{dx^2} + \frac{d\rho_0}{dx} \left(\frac{eE}{k_B T} + \frac{1}{\nu} \frac{d\nu}{dE} \frac{dE}{dx} \right) + \frac{e\rho_0}{k_B T} \left(\frac{dE}{dx} + \frac{E}{\nu} \frac{d\nu}{dE} \frac{dE}{dx} \right) = 0, \quad (5)$$

$$\frac{d^2 \boldsymbol{\rho}}{dx^2} + \frac{d\boldsymbol{\rho}}{dx} \left(\frac{eE}{k_B T} + \frac{1}{\nu} \frac{d\nu}{dE} \frac{dE}{dx} \right) + \frac{e\boldsymbol{\rho}}{k_B T} \left(\frac{dE}{dx} + \frac{E}{\nu} \frac{d\nu}{dE} \frac{dE}{dx} \right) + \frac{g\mu_B}{D\hbar} \mathbf{B} \times \boldsymbol{\rho} - \frac{\boldsymbol{\rho}}{D\tau} = 0. \quad (6)$$

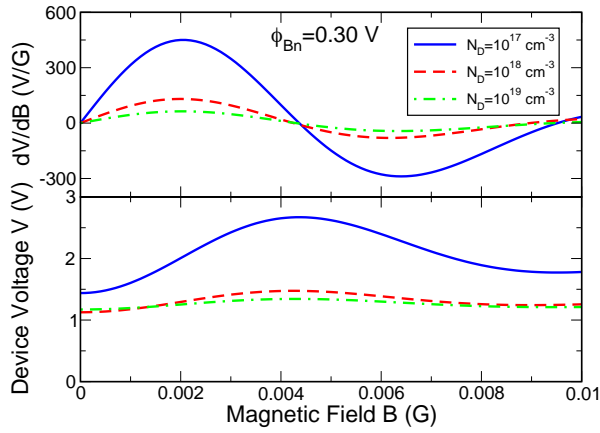


FIG. 3: Device sensitivity dV/dB (upper panel) and device voltage V (lower panel) as a function of applied magnetic field for different doping concentrations. The barrier height is 0.3 V. Other parameters are the same as in Fig. 2.

Here the carrier mobility is assumed to be a function of electric field, $\nu = \nu(E)$. Introducing chemical potentials \mathbf{f} for spins, $\boldsymbol{\rho} = \frac{e\rho_0}{k_B T} \mathbf{f}$, Eq. (6) can be rewritten as

$$\frac{d^2 \mathbf{f}}{dx^2} + \frac{d\mathbf{f}}{dx} \left(\frac{eE}{k_B T} + \frac{1}{\nu} \frac{d\nu}{dE} \frac{dE}{dx} \right) + 2 \frac{d \ln \rho_0}{dx} \frac{d\mathbf{f}}{dx} + \mathbf{h} \times \mathbf{f} - \frac{\mathbf{f}}{L^2} = 0, \quad (7)$$

where both \mathbf{h} and L are electric-field dependent through ν and D , $\mathbf{h} = g\mu_B \mathbf{B}/\hbar D(E)$ and $L = \sqrt{D(E)\tau_S}$.

Equations (5) and (7) represent the interdependent spin-charge transport equations, which need to be solved self-consistently with the Poisson's equation and proper boundary conditions.

III. ELECTRIC-FIELD DEPENDENT MOBILITY

Carrier mobilities in polymers often strongly depend on the electric field and are found to obey a universal Poole-Frenkel relation,

$$\nu = \nu_0 \exp \sqrt{\frac{E}{E_c}}, \quad (8)$$

where ν is the mobility and E_c measures how strong the field-dependence is. This Poole-Frenkel behavior originates from the disorders (traps) in the polymer. In a polymer with many carriers, as in these organic spin devices, the deep traps will likely be filled by the carriers, and the field-dependence is not so strong as in undoped or very lightly doped polymers. Using the Poole-Frenkel relation, we have

$$\frac{E}{\nu} \frac{d\nu}{dE} = \frac{1}{2} \sqrt{\frac{E}{E_c}}, \quad (9)$$

which will be used when solving Eqs. (5) and (7).

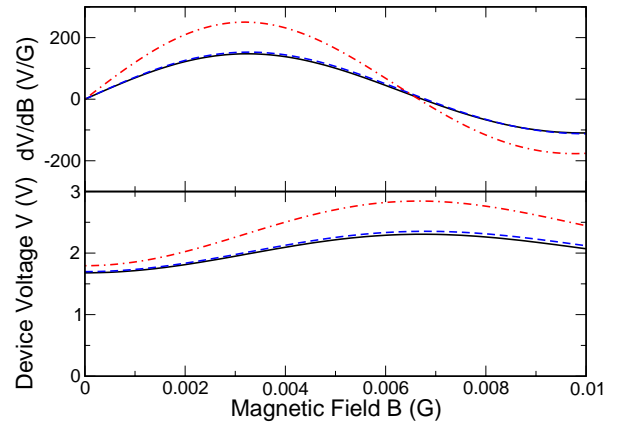


FIG. 4: Device sensitivity dV/dB (upper panel) and device voltage V (lower panel) as a function of applied magnetic field for values of N_C . The barrier height is 0.25 V. Other parameters are the same as in Fig. 2.

IV. SCHOTTKY BARRIER AND BOUNDARY CONDITIONS

The two magnets in a magnet-polymer-magnet can be regarded as magnetic reservoirs in local equilibrium at chemical potentials $\mu_{\mathcal{L},\mathcal{R}}^M$, which is diagonal in spin space $\hat{\mu}_{\mathcal{L},\mathcal{R}}^M = \mu_{\mathcal{L},\mathcal{R}}^M \hat{1}$. Here $\mathcal{L}(\mathcal{R})$ denotes the left (right) magnet. The direction of the magnetization in each magnet is described by the unit vector $\mathbf{m}_{\mathcal{L},\mathcal{R}}$. In the absence of Schottky barrier effects the current leaving the left contact at $x = 0$ and the current entering the right contact at $x = d$ are^{9,10}

$$\hat{j}^C(0) = G_0^\uparrow \hat{u}_{\mathcal{L}}^\uparrow [\hat{\mu}_{\mathcal{L}}^M - \hat{\mu}^P(0)] \hat{u}_{\mathcal{L}}^\uparrow + G_0^\downarrow \hat{u}_{\mathcal{L}}^\downarrow [\hat{\mu}_{\mathcal{L}}^M - \hat{\mu}^P(0)] \hat{u}_{\mathcal{L}}^\downarrow - G_0^{\uparrow\downarrow} \hat{u}_{\mathcal{L}}^\uparrow \hat{\mu}^P(0) \hat{u}_{\mathcal{L}}^\downarrow - G_0^{\downarrow\uparrow} \hat{u}_{\mathcal{L}}^\downarrow \hat{\mu}^P(0) \hat{u}_{\mathcal{L}}^\uparrow \quad (10)$$

$$\hat{j}^C(d) = G_0^\uparrow \hat{u}_{\mathcal{R}}^\uparrow [\hat{\mu}^P(d) - \hat{\mu}_{\mathcal{R}}^M] \hat{u}_{\mathcal{R}}^\uparrow + G_0^\downarrow \hat{u}_{\mathcal{R}}^\downarrow [\hat{\mu}^P(d) - \hat{\mu}_{\mathcal{R}}^M] \hat{u}_{\mathcal{R}}^\downarrow + G_0^{\uparrow\downarrow} \hat{u}_{\mathcal{R}}^\uparrow \hat{\mu}^P(d) \hat{u}_{\mathcal{R}}^\downarrow + G_0^{\downarrow\uparrow} \hat{u}_{\mathcal{R}}^\downarrow \hat{\mu}^P(d) \hat{u}_{\mathcal{R}}^\uparrow. \quad (11)$$

Here $\hat{\mu}^P$ is the polymer electrochemical potential in the spin space. Operators $\hat{u}_{\mathcal{L}}^{\uparrow(\downarrow)} = \frac{1}{2} [1 + (-)\hat{\boldsymbol{\sigma}} \cdot \mathbf{m}_{\mathcal{L}}]$ and $\hat{u}_{\mathcal{R}}^{\uparrow(\downarrow)} = \frac{1}{2} [1 + (-)\hat{\boldsymbol{\sigma}} \cdot \mathbf{m}_{\mathcal{R}}]$ project spins to the magnetization directions of the magnets. The above equations can be regarded as a generalized Ohm's law in the spin space. G_0^\uparrow (G_0^\downarrow) is the electron conductance in the magnet with spin parallel (antiparallel) to the magnetization direction. $G_0^{\uparrow\downarrow} = \text{Re}G_0^{\uparrow\downarrow} + i\text{Im}G_0^{\uparrow\downarrow}$ is the mixing conductance, which measures the transport capability of spins oriented perpendicular to the magnetization direction.

In a magnet-polymer-magnet structure, generally speaking, a Schottky barrier, as well as a depletion layer, will be formed at the interface between the magnet and polymer, which can significantly modify charge transport and electric-field distribution inside a device. The Schottky barrier height in a metal-semiconductor junction is

$$\phi_{Bn} = \phi_m - \chi \quad (12)$$

where $e\phi_m$ is metal work function, and $e\chi$ is the electron affinity measured from the bottom of the conduction band. Due to the image force, the Schottky barrier is lowered,

$$\tilde{\phi}_m = \phi_m - \sqrt{\frac{eE(0)}{4\pi\epsilon}}. \quad (13)$$

where $E(0)$ is the electric field at the boundary. The barrier reduction only occurs when the direction of $E(0)$ is pointing from the metal to the semiconductor. The current across a barrier consists of a contribution from thermionic emission and electron tunneling, which leads to a spin-dependent interfacial conductance. The up-spin conductance is

$$G_*^\uparrow = A^*T^2 \left[\exp\left(-\frac{e\tilde{\phi}_{Bn}}{k_B T}\right) + \exp\left(-\frac{e\phi_{Bn}}{E_{00}}\right) \right] \frac{e}{k_B T} \quad (14)$$

where the first term is from the thermionic-emission and the second is from the tunneling.

$$E_{00} = \frac{e\hbar}{2} \sqrt{\frac{N_D}{\epsilon m^*}} \quad (15)$$

The Richardson constant A^* is given by

$$A^* = \frac{4\pi\epsilon m^* k^2}{h^3} \quad (16)$$

where m^* is the electron effective mass of the polymer and measures the effectiveness of tunneling, which depends on both the doping concentration N_D and m^* . The total conductance at the magnet-polymer interface is then

$$G^\uparrow = (1/G_0^\uparrow + 1/G_*^\uparrow)^{-1}. \quad (17)$$

If the difference between G_0^\uparrow and G_0^\downarrow is due mainly to the energy gap between up-spin and down-spin electrons in the magnet, as in most half metals, the relations for conductance G_0 with difference spins would remain valid for G with different spins, $G^\uparrow/G^\downarrow = G_0^\uparrow/G_0^\downarrow$ and $G^{\uparrow\downarrow}/G^\uparrow = G^{\uparrow\downarrow}/G_0^\uparrow$.

Inside the polymer, the currents of spin and charge can be expressed as

$$j_0 = e\rho_0\nu E + \nu k_B T \frac{d\rho_0}{dx} \quad (18)$$

$$\mathbf{j} = -\frac{e^2\rho_0\nu E}{k_B T} \mathbf{f} - \nu e \frac{d\rho_0}{dx} \mathbf{f} - e\nu\rho_0 \frac{d\mathbf{f}}{dx}. \quad (19)$$

Substituting the four spin-dependent components of G_0 in Eqs. (8) and (9) by those of G , we have obtained a set of new boundary conditions for the magnet-polymer-magnet structure with a Schottky barrier.

The condition of a continuous current is not sufficient to determine the charge distribution in the depletion region of a Schottky barrier. One must specify the charge

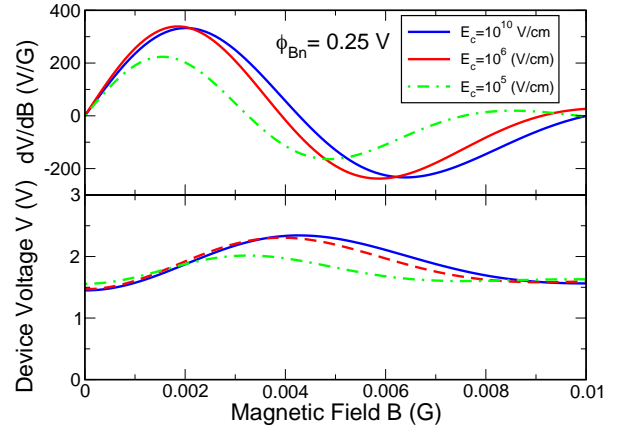


FIG. 5: Device sensitivity dV/dB (upper panel) and device voltage V (lower panel) as a function of applied magnetic field for different E_c , which measures how sensitive the mobility depends on the field. The barrier height is 0.25 V. Other parameters are the same as in Fig. 2.

density of the polymer at the at the boundary between the magnet and the polymer,

$$\ln\left(\frac{\rho}{\rho_c}\right)\Big|_{x=0} = \frac{-e\phi_{Bn} + e\sqrt{\frac{eE(0)}{4\pi\epsilon}}}{k_B T}, \quad (20)$$

$$\ln\left(\frac{\rho}{\rho_c}\right)\Big|_{x=d} = \frac{-e\phi_{Bn}}{k_B T}. \quad (21)$$

where $E(0)$ is the electric field at $x = 0$, which reduces the barrier height through the image charge, ρ_c is the effective density of state in the semiconductor, which is proportional to $(m^*)^{3/2}$. m^* in a polymer is usually larger than in an inorganic semiconductor, such as Si.

V. RESULTS

We have developed an efficient and accurate numerical approach to solve the coupled transport equations of spin and charge together with the Poisson equation. The magnetic contact is assumed to be LSMO, a half-metal, with a ratio of $G^\uparrow/G^\downarrow = 10^7$. We choose parameters pertinent to a realistic device structure. $\rho_c = 10^{21} \text{ cm}^{-3}$, which is considerably higher than in Si ($3.8 \times 10^{19} \text{ cm}^{-3}$). The corresponding carrier effective mass of the polymer is $m^* = 3.55m_0$, where m_0 is the bare electron mass. The Schottky barrier of 0.25 V is assumed. This is a typical energy difference between work functions of LSMO and MEH-PPV. From our calculation, a high barrier height larger than 0.5 V, would not allow even a decent charge injection from LSMO into a polymer.

Figure 1 illustrates the electric-field and carrier-density distributions of a LSMO-polymer-LSMO device. With a value of E_c set 10^{10} V/cm , the mobility is essentially independent of the field. We see that a depletion layer is

formed at both interfaces and the electric field in the depletion layers significantly deviates from the value in the middle of the device. Note that the two depletion layers are not symmetric because in the sandwiched structure considered here one Schottky barrier is under a forward bias and the other is under a reverse bias.

We plot in Figure 2 the device sensitivity dV/dB for different doping concentrations N_D . For a chosen barrier height of 0.25 V, we see that the dV/dB value obtained in $N_D = 10^{18} \text{ cm}^{-3}$ case is larger than that obtained in the case of either $N_D = 10^{17}$ or 10^{19} cm^{-3} . Since the average electric field as well as other parameters is fixed in these calculations for these doping levels, a larger dV/dB value indicates a higher spin injection efficiency from LSMO into the polymer. For a slightly different barrier height of 0.3 V, note from Figure 3 that the dV/dB value is larger for $N_D = 10^{17} \text{ cm}^{-3}$ than for $N_D = 10^{18}$ or 10^{19} cm^{-3} . As N_D increases, the Fermi level in the polymer moves closer to the conduction band edge. The effective barrier height increases and consequently the thermionic-emission current is reduced while the tunneling current is enhanced, which modifies dV/dB . Thus the above results indicate that spin injection can be enhanced by engineering Schottky barrier properties such as the barrier height and the doping in the semiconductor.

Figure 4 compares results with different N_C for a barrier height of 0.25 V. The values dV/dB for $N_C = 5 \times 10^{21}$ and 10^{21} cm^{-3} are similar, but are quite different from those for $N_C = 2 \times 10^{20} \text{ cm}^{-3}$. A smaller N_C means a smaller carrier effective mass, which would result in a larger tunneling current. The reduced dV/dB for $N_C = 2 \times 10^{20} \text{ cm}^{-3}$ suggests that when effective electron tunneling (smaller effective mass) is larger, the spin injection is reduced. We describe the effect of the field-dependent mobility on the device performance in Figure 5. We see that this effect becomes notable only when E_c is 10^5 V/cm , and even then dV/dB is not significantly affected. $E_c = 10^5 \text{ V/cm}$ is a typical value for undoped polymers and denotes a very strong electric-field depen-

dence of the mobility. It appears that field dependence in the cases of doped polymers will not play a significant role. The weak effect of field-dependent mobility on the device performance is possibly because the electric field is largely homogeneous inside the device except in the depletion layers.

In conclusion, our results, which are based on the realistic and accurate modeling that includes Schottky barrier effects as well as field dependence of the mobility, have demonstrated the robustness of the performance predicted from a simplified model. This model also suggests new degrees of freedom, such as the barrier height, carrier effective mass, and doping concentrations, to be engineered to achieve high performance of organic spin devices.

VI. CONCLUSIONS

We have presented a comprehensive theory to describe spin transport in magnet-polymer-magnet structures. This theory considers both the electric-field-induced spin drift and magnetic-field-induced spin precession. Our results, which are based on the realistic and accurate modeling that includes Schottky barrier effects as well as field dependence of the mobility, have demonstrated the robustness of the performance predicted from a simplified model. This model also suggests new degrees of freedom, such as the barrier height, carrier effective mass, and doping concentrations, to be engineered to achieve high performance of organic spin devices.

Acknowledgments

We thank Drs. M. A. Berding, E. Nowak, H. Katz, and J. Shi for helpful discussions. This work was supported by the Defense Advanced Research Projects Agency through the U.S. Army Research Office under contract W911NF06C0183.

* Electronic address: zhi-gang.yu@sri.com

¹ See, e.g., S. A. Wolf *et al.*, Science, **294**, 1488 (2001), and references therein.

² J. M. Kikkawa and D. D. Awschalom, Nature (London) **397**, 139 (1999).

³ V. Dediu, M. Murgia, F. C. Matocotta, C. Taliani, and S. Barbanera, Solid State Commun. **122**, 181 (2002).

⁴ Z. H. Xiong, D. Wu, Z. V. Vardeny, and J. Shi, Nature (London) **427**, 821 (2004).

⁵ See, for example, I. H. Campbell and D. L. Smith, Solid State Phys. **55**, 1 (2001).

⁶ Z. G. Yu, M. A. Berding, and S. Krishnamurthy, J. Appl.

Phys. **97**, 024510 (2005); Phys. Rev. B **71** 060408 (R) (2005).

⁷ Z. G. Yu and M. E. Flatté, Phys. Rev. B **66**, 201202 (R); **66**, 235302 (2002).

⁸ I. Appelbaum, B. Huang, D. J. Monsma, Nature **447**, 295 (2007).

⁹ A. Brataas, Yu. V. Nazarov, and G. E. W. Bauer, Phys. Rev. Lett. **84**, 2481 (2000).

¹⁰ D. H. Hernandez, Yu. V. Nazarov, A. Brataas, and G. E. W. Bauer, Phys. Rev. B **62**, 5700 (2000).

Appendix B

Realistic modeling of nonlinear absorption and transmission in semiconductor alloys

Srini Krishnamurthy^a and Zhi Gang Yu
SRI International, Menlo Park, CA 94025, USA

Shekhar Guha

Air Force Research Laboratory, Materials and Manufacturing Directorate, Wright-Patterson AFB, Ohio 45433

Leonel P. Gonzalez

General Dynamics Information Technology, Dayton, Ohio 45433

(Dated: December 10, 2007)

We have developed a code to study nonlinear propagation of high intensity light through semiconductor compounds and alloys. Nonlinear absorption and refraction are included. The input parameters— absorption and refraction coefficients, temperature and carrier densities— are inter-dependent and change in the sample as the light propagates. Using full bandstructures of GaAs, we evaluated all required parameters for 1.06 μm wavelength light. The transmission ratio of the output intensity to the input intensity, calculated without any adjustable parameter, agree very well with measured values. We further calculated the parameters for InP, Ga₆₄In₃₆As, and InP₆₀As₄₀ alloys to study the propagation of 1.55 μm wavelength light and predict largest attenuation of transmitted intensity in Ga₆₄In₃₆As alloy.

PACS numbers: 78.67.ch,42.65.k

Studies of nonlinear absorption (NLA) and nonlinear refraction (NLR) in semiconductors continues to be of scientific and technological interest.^{1,2} NLA is used in a number of applications, including frequency conversion, optical switches and optical limiting.¹ Consequently, the computer codes to model light propagation through the medium have been developed specifically for the chosen application.³⁻¹² The modeling of output intensity and beam profile variation with input intensity in semiconducting materials is being carried out for scientific as well as the selection of better materials for optical limiting applications.^{4,5} In these models, the NLA and NLR are characterized by two-photon absorption (TPA) and free carrier absorption (FCA) coefficients, and nonlinear refraction coefficients. However, in reality the values of these coefficients change as the light propagates through the material, owing to the creation of large number of photo-carriers and generation of heat. For example, when more carriers are generated, more band edge states are filled causing a drastic reduction in the TPA coefficients.^{13,14} Similarly, the changes in both carrier density and lattice temperature affect the magnitude and sign of the change in the refractive index.¹⁵⁻¹⁸ The computational method and code to study the beam propagation should include the transient nature of all nonlinear parameters.

In this Letter, we (a) outline the method used in our studies of beam propagation through nonlinear medium in three-dimensions, (b) use all inter-dependent parameters calculated from full bandstructures of GaAs, (c) demonstrate excellent agreement between the calculated transmission and measured values, and (d) apply this method to study the propagation of 1.55 μm light beam through GaAs, InP, Ga₆₄In₃₆As, and InP₆₀As₄₀ alloys. While the limiting is larger in smaller gap materials, we

predict higher performance in Ga₆₄In₃₆As alloy than that in InP₆₀As₄₀ alloy of nearly equal band gap.

The details of the calculational method for propagation will be published elsewhere.¹⁹ Here we give a brief outline for continuity. Since the study of three dimensional propagation of light requires both magnitude and phase of the electric field, we start from the form of Maxwell's equation, instead of the rate equation, and include nonlinear polarization term.²⁰

$$\begin{aligned}\nabla^2 E(\mathbf{r}, t) &= -\mu \left[\epsilon \frac{\partial^2 E(\mathbf{r}, t)}{\partial t^2} + \sigma_c \frac{\partial E(\mathbf{r}, t)}{\partial t} + \frac{\partial^2 P_{NL}(\mathbf{r}, t)}{\partial t^2} \right] \\ P_{NL}(\mathbf{r}, t) &= 3\epsilon_0 \chi^{(3)}(\omega, \omega, -\omega) |E(\mathbf{r}, t)|^2 E(\mathbf{r}, t)\end{aligned}\quad (1)$$

We assume $\mu = \mu_0$, and $\epsilon = n^2 \epsilon_0$, where μ_0 and ϵ_0 as the permeability and permittivity of the free space respectively and n is the refractive index of the medium. In the presence of FCA, the conductivity σ_c changes to $\sigma_{c0} + \Delta\sigma_c$ and n changes to $n_0 + \Delta n$, where the subscript 0 denote the corresponding value in the unperturbed medium. We then substitute $E(\mathbf{r}, t) = A(\mathbf{r}) e^{-ikz} e^{-i\omega t}$ in Eq. 1 and use the relationships between the one photon absorption coefficient α and σ , the nonlinear refractive index γ and the real part of the third-order susceptibility $\chi^{(3)}$, and the TPA coefficient β and the imaginary part of $\chi^{(3)}$ to get

$$\begin{aligned}\frac{\partial A}{\partial z} &= -\frac{A}{2} \left[\alpha_0 + \alpha_f + \beta I \left(1 - \frac{\Delta n}{n_0} \right) \right] + \frac{i \nabla_T^2 A}{2k_0} \\ &\quad - \frac{ik_0 A}{n_0} \left[\Delta n + \gamma I \left(1 - \frac{\Delta n}{n_0} \right) \right] + O(\Delta^2)\end{aligned}\quad (2)$$

The subscript T denotes the transverse-to-propagation direction and the corresponding component in the prop-

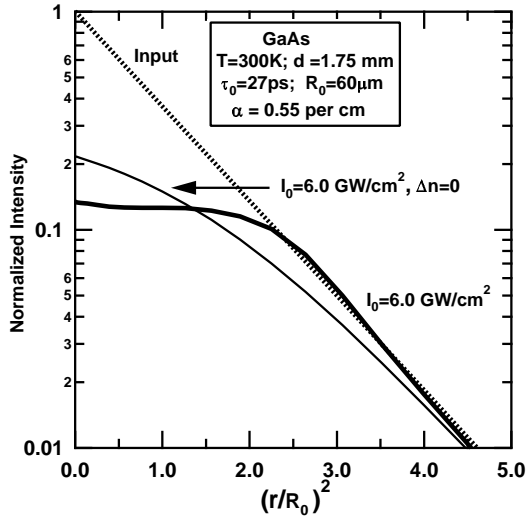


FIG. 1: Radial distribution of the beam just inside the entry surface (dotted line) and exit surface with (thick solid line) and without (thin solid line) refraction terms. Input pulse is normalized to 1 at the the beam center

agation direction is assumed to be zero (paraxial approximation). α_f is the FCA coefficient, and k_0 is the wavevector in the unperturbed medium. The first term determines the magnitude, whereas the second and third terms determine the phase of the electric field of the propagating wave. Eq. 2 is solved on a three-dimensional numerical mesh by rewriting it in an implicit form and care is taken to achieve numerical stability by using staggered-leapfrog differencing scheme. With measured incident pulse profile as the initial boundary condition, the beam profile at the exit surface is calculated as a function of time and radial distance by solving Eq.2 self-consistently with the rate equations^{13,14} governing the photo-generated carrier density (ΔN) and temperature (T) in the sample. The propagation of the beam profile from the exit surface to the aperture is calculated in Hankel function approach²¹ and integrated as appropriate for closed or open aperture measurements.

An important ingredient in our beam propagation modeling is the use of β , α_f , and Δn , calculated from full bandstructures, along with their complicated dependence¹⁴ on ΔN and T . Since ΔN and T depends on \mathbf{r} and t , these parameters are continuously evaluated and used in the equations as the beam propagates through the sample. Our previous calculations in the midwave infrared (MWIR) regime indicates strong variation of the parameters β and FCA cross section σ (which is the ratio of FCA coefficient to carrier density) with T and ΔN . The calculations carried out here in the 1.06 μm to 1.55 μm regime also indicate strong variation with T , but not with ΔN for densities up to 10^{18} cm^{-3} .

The nonlinear parameters (β , σ , and Δn) in GaAs are calculated as described previously from the underlying tight-binding bandstructures.²² At MWIR wavelengths,

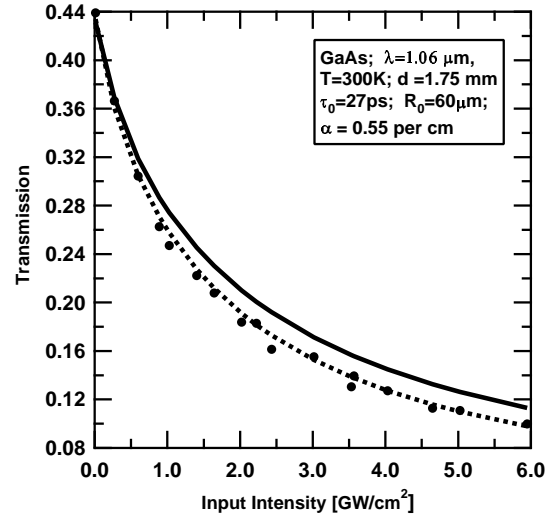


FIG. 2: The transmission calculated without any adjustable parameter (solid line) is compared to the measured values (data). The value of β adjusted to yield good fit (dashed line) is 22 cm/GW

the value of β and σ in semiconductors are of the order of 1 cm/MW and 10^{-16} cm^2 . However, the corresponding values at 1.06 μm wavelength in intrinsic GaAs are calculated to be $1.8 \times 10^{-2} \text{ cm/MW}$ (or 18 cm/GW) and $7.1 \times 10^{-20} \text{ cm}^2$ at 300K. Since the material is required to have larger band gap for nonlinear absorption at shorter wavelengths, the β is very small. The FCA cross section is small because of the holes, which play a dominant role in FCA at MWIR wavelengths, can not participate in the absorption of short wavelength photons. In other words, the electrons in light-hole valence band do not find a final state at the same wavevector \mathbf{k} in heavy hole band after the direct absorption of 1.2 eV photons. Both electrons in the conduction band and holes in the valence bands contribute to FCA only through an indirect process, with the assistance from phonons, and hence the cross section is extremely small.

The calculated nonlinear parameters at 1.06 μm are used in the beam propagation model to study the transmission of laser pulse with half-width at 1/e of the maximum (HW1/eM) of 27 ps and 60 μm . These beam parameters, the sample thickness (of 0.175 cm) and incident intensity values are taken from Ref.²³. The sample is not anti-reflection (AR) coated. A measured²⁴ value of $-4.1 \times 10^{-16} \text{ cm}^2/\text{W}$ for γ is used. The incident beam just inside the GaAs entry surface is shown in Fig. 1 by dotted line. Also shown are the calculated beam profile at the exit surface with (thick solid line) and without (thin solid line) the refraction terms. Since the absorption is proportional to intensity, more of the light is absorbed at the center of the beam. Hence we see that even when the refraction is not considered, the transmitted beam is non-gaussian. In the presence of refraction, the beam spreads additionally and away from the center, resulting

TABLE I: Calculated nonlinear parameters in intrinsic material at $T=300\text{K}$ and $\lambda=1.55\mu\text{m}$

Parameters	GaAs	InP	$\text{InP}_{60}\text{As}_{40}$	$\text{Ga}_{64}\text{In}_{36}\text{As}$
β [cm/GW]	7.3	12.3	32.9	36.2
σ [10^{-20}cm^2]	21.6	14.7	23.0	22.1
dn/dN [10^{-21}cm^3]	-1.05	-2.3	-15.9	-16.2
dn/dT [10^{-4}K^{-1}]	1.3	0.54	2.1	2.5

in highly non-gaussian beam profile as shown.

The transmitted output energy is simply the time and radial integration of beam profile at the exit surface. The transmission coefficient, which is the ratio of output energy to input energy, calculated with full bandstructure parameters is plotted (thick solid line) in Fig. 2 as a function of input intensities. Both trend and magnitude compare well with the measured values (filled circles).²³ However, when the β value of 18 cm/GW at 300K is slightly increased to 22 cm/GW, we can obtain a near perfect fit (dashed line) with experimental values. Hence we conclude that both calculated and experimental values agree very well within the numerical and measurement accuracies.

The calculations are then carried out to predict materials' limiting performance at $\lambda=1.55\mu\text{m}$. For the comparative study, we considered GaAs and InP compounds and $\text{Ga}_{64}\text{In}_{36}\text{As}$ and $\text{InP}_{60}\text{As}_{40}$ alloys. GaAs and InP have near equal bandgap of 1.42 eV and 1.35 eV respectively at 300K. The alloy concentrations in $\text{Ga}_{64}\text{In}_{36}\text{As}$ and $\text{InP}_{60}\text{As}_{40}$ are chosen so that they have equal band gap (of 0.92 eV) at 300K. The nonlinear parameters β , σ , dn/dN , and dn/dT obtained from underlying bandstructures at 300K are given in Table I. We note that the β in GaAs is reduced when the wavelength is increased from 1.06 to 1.55 μm , and that it increases when the bandgap is decreased. Although the bandgap in InP is nearly equal to that in GaAs, the calculated β differs by as much as 50%. In spite of near-identical bandgap value in the alloys, the β differ by about 10%. The FCA cross section is known²⁵ to vary as λ^3 and we see that the calculated σ in GaAs follows that variation. We further find that σ is nearly independent of the bandgap of materials considered. As before, their variation with T and ΔN are also calculated and used in our code. For simplicity, the incident beam profile is assumed to be Gaussian with temporal and spatial HW1/eW of 27 ps and 60 μm respectively, the sample is not AR coated and has a thickness of 1.75 mm (all parameters, except wavelength, are identical to those used to obtain Fig. 1 and 2). The transmission coefficients obtained as functions of incident intensity in GaAs, InP, $\text{Ga}_{64}\text{In}_{36}\text{As}$ and

$\text{InP}_{60}\text{As}_{40}$ are shown in Fig. 3. Because of the difference in the refractive index (of 3.31 in GaAs and 3.1 in InP) and the resulting Fresnel reflection, the transmission at low intensities in GaAs and InP are different. At higher intensities, InP is expected to limit better than GaAs. In general, we see that the limiting at a given wavelength is enhanced with the reduction in the bandgap. Considerably enhanced limiting performance is predicted in $\text{InP}_{60}\text{As}_{40}$ and $\text{Ga}_{64}\text{In}_{36}\text{As}$ alloys. Owing to slightly larger β , the $\text{Ga}_{64}\text{In}_{36}\text{As}$ alloy is predicted to offer the best optical limiting performance at this wavelength. We call for experimental verification of this prediction.

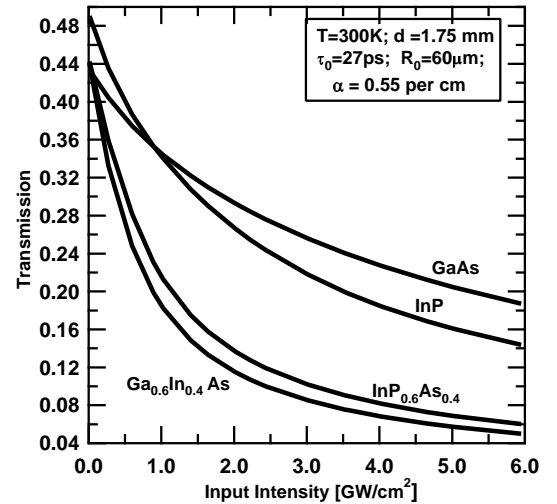


FIG. 3: Calculated transmission of 1.55 μm beam through GaAs, InP, $\text{Ga}_{64}\text{In}_{36}\text{As}$ and $\text{InP}_{60}\text{As}_{40}$ as a function of incident intensity.

In summary, we have developed a method to study the beam propagation in three dimension by including nonlinear absorption and refraction. When the interdependent nonlinear parameters obtained from full bandstructures are used in the code, an excellent agreement with measured transmission of 1.06 μm beam through GaAs. The further calculations carried out for 1.55 μm beam predict a superior limiting performance in $\text{InP}_{60}\text{As}_{40}$ and $\text{Ga}_{64}\text{In}_{36}\text{As}$ alloys, with GaInAs offering a slightly better performance.

The authors (SK and ZY) gratefully acknowledge the financial support from US Air Force through General Dynamics Information Technology contract (USAF-5408-19-SC-0009) and from DARPA through ARO contract (W911NF-06-C-0183).

^(a)srini@sri.com

¹ For a review, E. Garmire, IEEE J. on Selected Topics in Q. Elec., **6**, 1094 (2000) and the references cited therein.

² B. Jenson, *Infrared and millimeter waves*, Ed. K. Button

(Academic, New York, 1982), Vol. 8.

³ C. Pare and P.-A. Belanger, Opt. and Quan. Elec. **24**, S1051 (1992)

- ⁴ D. Kovesh, S. Yang, D.J. Hagen, E.W. Van Stryland, *Non-linear Optical Liquids for power limiting and imaging* (Ed. C.M. Lawson), Proc. SPIE **3472**, 163 (1998).
- ⁵ D. Kovesh, S. Yang, D.J. Hagen, E.W. Van Stryland, Appl. Opt. **38**, 5168 (1999).
- ⁶ Q. Guo and S. Chi, J. Pure Appl. Opt. **2**, 5 (2000)
- ⁷ S. Mou, C-F. Lin, H.F. Chou, J. Lightwave Tech. **19**, 772 (2001).
- ⁸ P. Milsom, G. Bourhill, and J. Robertson, Lasers and Electro Optic Society, 14th Annual Meeting of the IEEE, **2**, 445 (2001).
- ⁹ A. Eriksson, K. Bertilsson and M. Lindgren Synt. Metals, **127**, 147(2002).
- ¹⁰ A. Locatelli, D. Modotto, C. Angelis, F.M. Pigozzo, and A.D. Capobianco, J. Opt. Soc. Am. B **20**, 1724 (2003).
- ¹¹ T. Fujisawa and M. Koshiba, J. Lightwave Tech. **22**, 684 (2004).
- ¹² W. Zang, J. Tian, Z. Liu, W. Zhou, F. Song, and C. Zhang, Opt. Comm. **256**, 210 (2005)
- ¹³ S. Krishnamurthy, Z.G. Yu, L.P. Gonzalez, and S. Guha Appl. Phys. Lett. **89**, 161108 (2006)
- ¹⁴ S. Krishnamurthy, Z.G. Yu, L.P. Gonzalez, and S. Guha J. Appl. Phys. **101**, 113104 (2007)
- ¹⁵ Z.G. Yu, S. Krishnamurthy, and S. Guha J. Opt. Soc. Am. **B 23**, 2356 (2006)
- ¹⁶ For a review, D. Kovesh, S. Yang, D.J. Hagen, E.W. Van Stryland, SPIE **3472**, 163 (1998).
- ¹⁷ M. Sheik-Bahae, D.C. Hutchings, D.J. Hagen, and E.W. Van Stryland, IEEE J. Quan. Elec. **27**, 1296(1991).
- ¹⁸ D.A.B. Miller, C.T. Seaton, M.E. Prise, and S.D. Smith, Phys. Rev. Lett. **47**, 197 (1981)
- ¹⁹ S. Krishnamurthy, Z.G. Yu, L.P. Gonzalez, and S. Guha (in preparation for publication)
- ²⁰ P. B. Chapple, J. Staromlynska, J. A. Hermann and T. J. Mckay, J. Nonlin. Opt. Phys. and Mater. **6**, 251 (1997).
- ²¹ M. Born and E. Wolf, *Principles of Optics*, 5th ed. (Pergamon, Oxford, 1975), p. 383.
- ²² A.-B. Chen and A. Sher, *Semiconductor Alloys*, ch.7 (Plenum, New York, 1995).
- ²³ T.F. Boggess, A.F. Smirl, S.C. Moss, I.W. Boyd, and E.W. van Stryland, IEEE J. Quan. Elec. **21**, 488 (1985).
- ²⁴ A.A. Said, M. Sheik-Bahae, D.J. Hagen, T.H. Wei, J. Wang, J. Young, and E. Van Stryland, J. Opt. Soc. Am. B **9**, 405 (1992).
- ²⁵ J.I. Pancove, *Optical processes in Semiconductors*, (Dover, New York, 1975), p. 75.